Available online at www.sciencedirect.com

ScienceDirect

journal homepage: www.elsevier.com/locate/AJPS



Research Article

Porous Baicalin-Fe(III) ICP@Propofol nanocomposites for enhanced anesthetic efficacy and reduced toxicity via neuroprotection and ultrasound assistance

Shuo Zhang[a], *Lei Shi*[c], *Jiansheng He*[c], *Ji Xia*[c], *Shunlian Li*[c], *Rong Wang*[b], *Qingyan Ma*[a], *Mingting Zhu*[b], *Peng Tang*[b], *Hao Tian*[c], *Feiqian Wang*[c], *Mingxi Wan*[b], *Daocheng Wu*[b,*], *Wei Gao*[c,*], *Xiancang Ma*[a,*], *Feng Zhu*[a,*]

[a] *Department of Psychiatry, Center for Brain Science, Center for Translational Medicine, The First Affiliated Hospital of Xi'an Jiaotong University, Xi'an 710061, China*

[b] *The Key Laboratory of Biomedical Information Engineering of Ministry of Education, School of Life Science and Technology, Xi'an Jiaotong University, Xi'an 710049, China*

[c] *Department of Anesthesiology, the First Affiliated Hospital of Xi'an Jiaotong University, Xi'an 710061, China*

ARTICLE INFO

Article history:
Received 2 July 2025
Revised 18 August 2025
Accepted 3 September 2025
Available online 11 January 2026

Keywords:
Propofol
Baicalin
Infinite coordination polymer
Neuroprotection
Ultrasound

ABSTRACT

To enhance the anesthetic efficacy of propofol while mitigating its systemic toxicity and irreversible developmental neurotoxicity, we developed a strategy leveraging the neuroprotective effects of baicalin in combination with propofol anesthesia via baicalin-based nanocomposites. High propofol-loaded porous Baicalin-Fe(III) infinite coordination polymer@propofol nanocomposites were synthesized, wherein baicalin coordinates with Fe^{3+} ions to form porous nanoparticles that encapsulate propofol within a core-shell structure. These nanocomposites exhibited an average diameter of 92.3 ± 10.2 nm and a pore volume of 0.322 cm^3/g, achieving ultra-high propofol loading (~62%) with no detectable leakage over 100 d, attributed to their large surface area and strong molecular interactions. When combined with focused ultrasound (FUS) and microbubbles, the effective dose (ED_{50}) of propofol decreased from 10 to 4.3 mg/kg, doubling the duration of anesthesia and extending the therapeutic window by 200%. Importantly, the therapeutic index improved 1.66-fold while vital physiological parameters remained stable. Histological analyses revealed an 80% reduction in neuronal injury compared to free propofol, and behavioral tests demonstrated significant enhancements in motor and cognitive performance, alongside recovery from propofol-induced irreversible developmental neurotoxicity, indicating effective neuroprotection. Collectively, this baicalin-propofol nanocomposite, coupled with

* Corresponding authors.
E-mail addresses: wudaocheng@mail.xjtu.edu.cn (D. Wu), 545359725@qq.com (W. Gao), maxiancang@163.com (X. Ma), zhufeng1982@xjtu.edu.cn (F. Zhu).

Peer review under responsibility of Shenyang Pharmaceutical University.

https://doi.org/10.1016/j.ajps.2026.101117

1818-0876/© 2026 Shenyang Pharmaceutical University. Published by Elsevier B.V. This is an open access article under the CC BY-NC-ND license (http://creativecommons.org/licenses/by-nc-nd/4.0/)

FUS-mediated delivery, represents a promising approach for safe and long-term anesthesia in clinical applications.

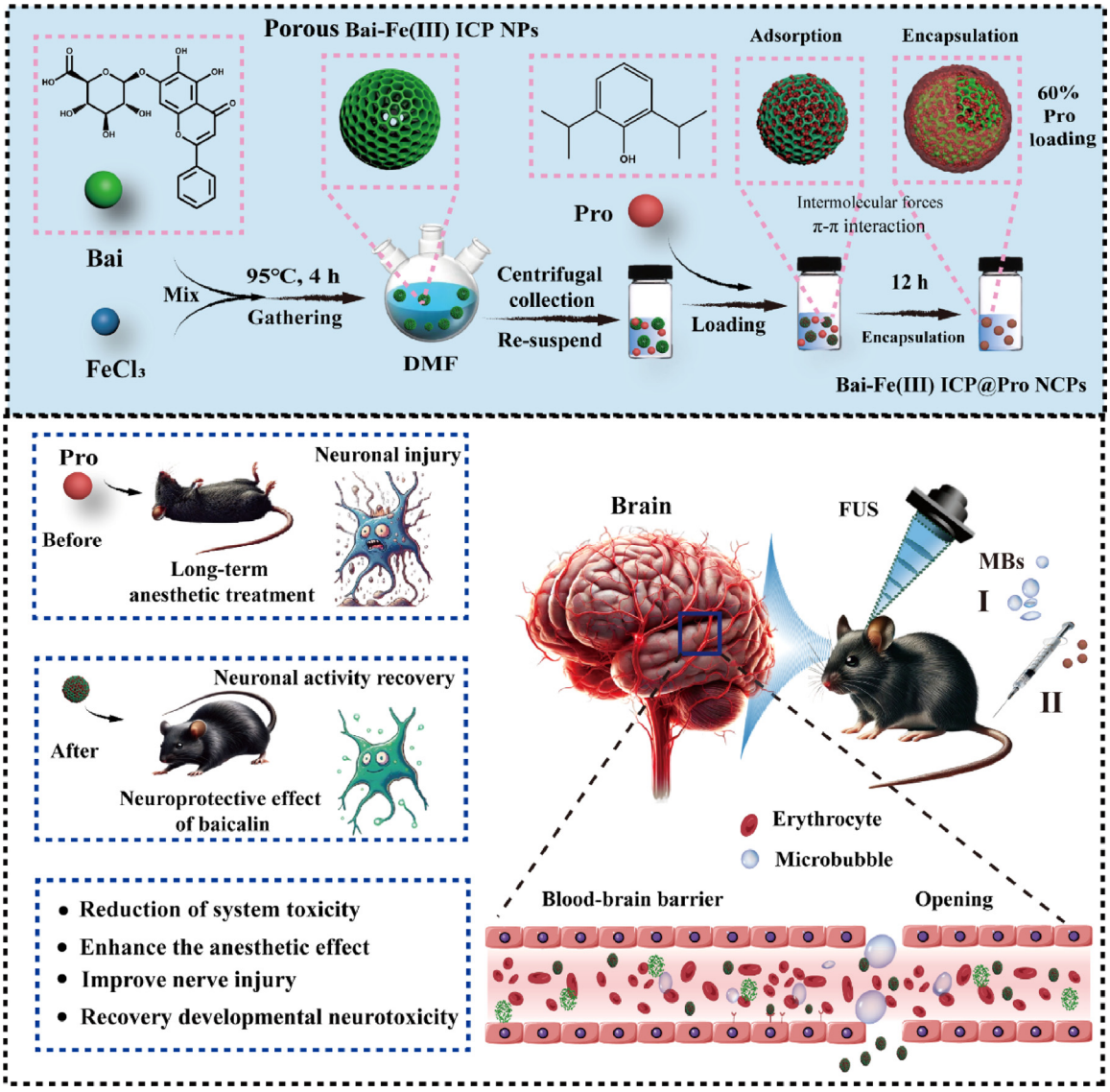
© 2026 Shenyang Pharmaceutical University. Published by Elsevier B.V.
This is an open access article under the CC BY-NC-ND license (http://creativecommons.org/licenses/by-nc-nd/4.0/)

1. Introduction

Propofol (Pro) is a widely used intravenous anesthetic known for its rapid induction, short recovery time and controllable depth of anesthesia [1–3], making it a mainstay in clinical practice for both induction and maintenance. However, despite these advantages, its clinical application is severely constrained by a narrow therapeutic window, significant systemic toxicity, and neuronal damage; prolonged or high-dose use can induce anxiety-like behavior, depression-like symptoms, motor deficits in pediatric patients, and irreversible neuronal damage in learning, memory, and neurocognitive function [4–6], posing substantial obstacles for clinical use. Mechanistic studies have demonstrated that propofol impairs hippocampal synaptic plasticity and induces neuronal apoptosis: for instance, Shi et al. reported that systemic administration of propofol inhibits long-term potentiation in hippocampal CA1 pyramidal neurons via enhanced GABAergic inhibitory transmission, ultimately leading to spatial memory deficits [7], while Yang et al. showed that propofol-induced neuronal apoptosis is mediated by the miR-34a/PI3K/Akt signaling pathway, triggering chromatin margination and nuclear condensation in hippocampal neurons [8]. Currently, propofol is delivered as a lipid-based emulsion to enhance solubility and facilitate blood-brain barrier (BBB) penetration [9–11]. However, these emulsions are limited by low drug-loading capacity, poor physical stability, and high susceptibility to bacterial contamination due to their lipid content [12–14], and they remain inadequate in fully mitigating propofol-induced neurotoxicity, highlighting the urgent need for improved delivery systems [15] (Scheme 1).

One strategy to address the limitations of propofol is composite anesthesia, wherein propofol is combined with other anesthetic agents to lower the required dosage of each drug [16]. However, this method presents new challenges, such as the toxicity of co-administered anesthetics and the need for precise, synchronized delivery of multiple drugs to the brain, a task hindered by the physicochemical incompatibilities among anesthetics in current emulsion systems [17–19]. Conventional propofol delivery systems, including polymeric and nanoparticle carriers, often suffer from low encapsulation efficiency and significant drug leakage *in vivo*, with alginate-based nanoparticles, for instance, achieving only a 0.2% loading capacity [20]. In our previous work, we employed the bridge molecule monoglyceride monooleate (GMO) and surfactant F127 to create molecular aggregates with propofol and etomidate through molecular interactions, increasing propofol loading to 16.7% and suggesting that such interactions can be an effective means of enhancing loading capacity [21]. While this method improved brain delivery of propofol, the loading efficiency remained suboptimal, and the process required complex assembly while introducing additional components, such as GMO and F127, which may be undesirable for clinical use. Consequently, there remains an urgent need for a biocompatible, high-loading propofol delivery system that can support composite anesthesia. A major barrier is the challenge of crossing the BBB. Focused ultrasound combined with microbubbles (FUS-MBs) has emerged as a clinically validated, non-invasive technique for transient BBB disruption [22–24], capable of enhancing central nervous system (CNS) drug accumulation by 4 to 6-fold without added toxicity and allowing repeated applications [25,26]. Our studies have shown that FUS-MBs can significantly enhance the anesthetic efficacy of propofol-etomidate molecular aggregates while reducing systemic exposure, demonstrating that FUS-MB-assisted delivery is a mature and effective approach for facilitating propofol's entry into the brain and improving its anesthetic action. Despite progress in mitigating the systemic toxicity and side effects of propofol, the improvements achieved thus far remain limited, primarily due to the absence of a delivery system with sufficiently high propofol loading, and there are virtually no reports on such systems addressing propofol-induced neural damage.

Recent studies have underscored the therapeutic promise of baicalin, a naturally occurring polyphenolic compound with a planar aromatic structure, widely employed in treating neurological disorders due to its potent neuroprotective and reparative effects [27–29]. For instance, Cao et al. demonstrated that baicalin mitigates cerebral ischemia-reperfusion injury by activating AMPK signaling and suppressing NLRP3 inflammasome-mediated pyroptosis, thereby reducing the release of pro-inflammatory cytokines [30], while Walder et al. reported that baicalin exerts anti-inflammatory effects, enhances mitochondrial function, and modulates TNF-α expression, ultimately improving ATP production and promoting neuronal survival [29]. Therefore, the most important neuroprotective mechanism of baicalin is enhancing antioxidant defenses via activation of the Nrf2/ARE pathway while inhibiting NF-κB–mediated inflammatory responses, thereby reducing damage caused by oxidative stress and neuroinflammation. These properties make baicalin a compelling candidate for CNS therapeutics, combining efficacy with safety. From a molecular design perspective, baicalin is particularly attractive as a drug carrier owing to its multiple hydroxyl groups facilitating hydrogen bonding formation and conjugated aromatic rings, which support diverse non-covalent interactions with small lipophilic molecules such as propofol [31]. Given that propofol also contains a phenolic hydroxyl group and an aromatic ring, it can readily interact with baicalin through hydrogen bonding, van der Waals forces, electrostatic



Scheme 1 – The schematic illustration of the design and preparation of Bai-Fe(III) ICP@Pro NCPs, with the help of US-MBs, significantly improving the efficiency of drug entry into the brain for effective anesthesia and neuroprotection. Propofol (Pro) and Baicalin (Bai).

attractions, hydrophobic effects, and π-π stacking [21], a relationship confirmed by molecular simulations (Fig. 1) showing stable molecular-level associations. Building on these insights, we hypothesized that baicalin could serve a dual function in a novel propofol delivery system, as both a functional carrier and a synergistic anesthetic agent, offering two key advantages: enhanced propofol loading efficiency via strong molecular interactions and reduced neurotoxicity through baicalin's neuroprotective synergy, thereby improving overall CNS outcomes. In this concept, baicalin acts not as a passive matrix but as an active molecular partner, amplifying propofol's anesthetic effects while mitigating its systemic toxicity and neuronal damage. Accordingly, we proposed a strategy harnessing baicalin's neuroprotective properties alongside propofol's anesthetic potency to enhance efficacy and minimize adverse effects. The principal design challenge lies in constructing a baicalin-based nanocarrier with high drug-loading capacity and strong *in vivo* stability [32–34]. Inspired by our prior research on propofol molecular aggregates, we developed a novel platform in which baicalin coordinates with Fe^{3+} ions to form porous infinite coordination polymer (ICP) nanocomposites, which subsequently encapsulate propofol in the outer layer through both structural confinement and molecular-level interactions. Owing to the porous structure greatly increasing the surface area of baicalin, it significantly increases the contact area between baicalin and propofol molecules and their intermolecular interactions. Therefore, unlike lipids and micelles that are prone to leakage and instability, the propofol loading capacity and stability can be greatly enhanced. This innovative design fully exploits baicalin's chemical compatibility, biofunctionality, and self-assembly capabilities to create a synergistic, high-performance propofol delivery system.

Given the small molecular weight and strong lipophilicity of propofol (hydrophobicity and rapid clearance), one of the major challenges in developing a propofol delivery system is achieving high drug loading and preventing premature leakage in aqueous environments. To address these limitations, we designed a novel delivery platform based on porous ICP nanoparticles, synthesized through the coordination of baicalin with Fe^{3+} ions. This design capitalizes on two critical features: (1) baicalin's capacity for strong intermolecular interactions with propofol via π-π stacking, hydrogen bonding, and hydrophobic forces, and (2) the large surface area and porosity of the ICP framework, which promote efficient molecular adsorption and retention. In this system, propofol is initially adsorbed within the porous interior of the baicalin-Fe^{3+} network, where spatial confinement and enhanced molecular interactions ensure secure encapsulation. Excess propofol then self-assembles on the outer surface of the porous nanoparticles, yielding a core-shell nanostructure. This dual-encapsulation strategy produces high-propofol-loading baicalin-iron(III) ICP nanocomposites (Bai-Fe(III) ICP@Pro NCPs), in which the interconnected network of internally and externally bound propofol molecules markedly enhances both the loading capacity and long-term stability of the formulation, effectively eliminating premature leakage. Molecular dynamics (MD) simulations demonstrated the formation of approximately 20 hydrogen bonds between baicalin and propofol within the nanocomposites, with a total binding free energy of −476 kcal/mol, compared to only 0–3 hydrogen bonds and −12 kcal/mol in the absence of the ICP framework, underscoring the nanocomposites' strong molecular cohesion essential for stability. Following encapsulation, the radius of gyration of the complex decreased, indicating that propofol was drawn into the nanoparticle's central cavity, while excess propofol on the surface assembled into a dense, stable layer, ensuring high loading and long-term non-leakage (Fig. 1). These results confirm the feasibility of creating a carrier-free, highly loaded propofol nanoplatform composed entirely of baicalin. To experimentally validate the concept, we synthesized porous baicalin-Fe^{3+} ICP nanoparticles by conducting the coordination reaction at 95 °C, a condition that promoted uniform nucleation and pore formation. The resulting nanocomposites displayed a distinct core-shell morphology with an average diameter of 92.3 ± 10.2 nm, a pore volume of 0.322 cm^3/g, and an average pore size of 5.1 ± 0.2 nm. This architecture enabled an exceptionally high propofol loading of approximately 62%, with no detectable leakage for over 90 d in aqueous solution, performance that far exceeds the stability and efficiency of conventional lipid-based emulsions and previously reported propofol delivery systems.

Anesthetic evaluation demonstrated the pronounced therapeutic benefits of the proposed nanocomposites. When combined with FUS and microbubbles (MBs), the effective dose (ED_{50}) of propofol was reduced from 10 to 4.3 mg/kg, while standard dosing resulted in a twofold increase in anesthesia duration and a 200% extension of the therapeutic window. The therapeutic index (TI) improved by 1.66-fold, and physiological parameters remained stable within normal ranges in murine models, underscoring the precision and clinical applicability of the formulation. Long-term biosafety assessment using a juvenile mouse model revealed that the neuronal injury score in the FUS-assisted nanocomposite group was only one-fifth of that observed in the free propofol group, indicating that baicalin within the nanocomposites markedly attenuates propofol-induced neuronal injury. Behavioral testing further confirmed these neuroprotective effects: in the open-field test, mice receiving free propofol traveled only 8 m in the central area, about one-third of the control group's distance (24 m), whereas mice treated with Bai-Fe(III) ICP@Pro NCPs or Bai-Fe(III) ICP@Pro NCPs+US maintained total distances exceeding 16 m. In recognition memory assessment, the recognition index (RI) for the free propofol group was approximately 2.9%, far lower than the control group's 13.5%, while the RI values for both nanocomposite-treated groups reached roughly 65% of control levels. Similarly, in novel object recognition and Y-maze tests, the free propofol group exhibited an alternation score of about 40%, reflecting a substantial reduction in spontaneous alternation behavior compared to the control group's 80%, whereas mice treated with Bai-Fe(III) ICP@Pro NCPs or Bai-Fe(III) ICP@Pro NCPs+US showed no significant difference from controls, with an alternation score of 69.8%. These findings confirm that the nanocomposites significantly improve both motor and cognitive performance, highlighting baicalin's synergistic neuroprotective role in mitigating irreversible developmental neurotoxicity caused by propofol. Overall, the rationally designed, high propofol loading Baicalin-Fe(III) infinite coordination polymer@ propofol nanocomposites, combined with a baicalin-based neuroprotective and propofol anesthesia strategy. This study aims to develop a baicalin-based nanocomposite for enhanced propofol delivery and neuroprotection and hold strong promise for future clinical anesthesia applications.

2. Materials and methods

2.1. Materials

Propofol and baicalin were purchased from Sigma-Aldrich Trading Co., Ltd. (Shanghai, China), while the near-infrared (IR) fluorescent dye IR780 was obtained from Caliper Life Sciences Inc. (Massachusetts, USA). Copper grids with carbon support films were sourced from Beijing Zhongjingkeyi Technology Co., Ltd. (Beijing, China). Dialysis membranes with molecular weight cut-off (MWCO) values of 3500 Da and 8000–14,000 Da were supplied by MYM Biological Technology Co., Ltd. (Maryland, USA). SonoVue MBs were provided by Bracco S.p.A. (Milan, Italy), and isoflurane for anesthesia was obtained from RWD Life Science Co., Ltd. (Shenzhen, China). All reagents were of analytical grade or higher and were used as received without further purification unless otherwise stated.

2.2. Cells and animals' model

Mouse hippocampal neuron cells (HT22) were obtained from Wuhan Puno Science Life Technology Co., Ltd. and cultured in dulbecco's modified eagle medium (DMEM) medium

supplemented with 10% fetal bovine serum at 37 °C in a CO_2 incubator (Thermo Forma 311, USA) with 5% CO_2. C57BL/6 mice (3–5 weeks old, 12–16 g) were purchased from the Department of Experimental Animals, Health Science Center, Xi'an Jiaotong University. All experimental protocols were approved by the Xi'an Jiaotong University Ethics Committee (No. 201929, approved on Dec 20, 2023), and every effort was made to minimize animal suffering. The animals were housed under controlled conditions with a 12 h light/dark cycle, and provided with food pellets and water ad libitum. Prior to all experiments, mice underwent 24 h of fasting with free access to water, under an environmental temperature of 22 ± 2 °C and relative humidity of 35% ± 10%).

2.3. *Methods of molecular simulation*

Molecular dynamics (MD) simulations of the complex were carried out using the GROMACS 2024 software package. The free drug molecule was parameterized using the General Amber Force Field 2 (GAFF2), which offers broad applicability for organic molecules and has been optimized to reproduce the structural and energetic properties of small drug-like compounds with high accuracy. Partial atomic charges were assigned using the AM1-BCC method as implemented in the ANTECHAMBER module, providing a balance between computational efficiency and reliable charge distribution for molecular simulations. System preparation was carried out using TLEAP, during which hydrogen atoms and appropriate counterions were added to neutralize the total system charge. The resulting system was solvated in an explicit TIP3P water model box, and periodic boundary conditions were applied in all three spatial dimensions to simulate bulk-phase behavior.

The MD simulations were conducted in four sequential stages: energy minimization, heating, equilibration, and production dynamics. Initially, positional restraints were applied to the heavy atoms of the complex, allowing only the solvent molecules to relax. This stage involved 10,000 steps of energy minimization, consisting of 5,000 steps using the steepest descent algorithm followed by 5,000 steps of conjugate gradient minimization. Subsequently, all restraints were removed, and the entire system underwent an additional 10,000 steps of full minimization to eliminate any residual steric clashes. The minimized system was then gradually heated from 0 K to 300 K over 50 ps under constant volume (NVT) conditions. Once the target temperature was reached, a 50 ps equilibration phase was performed in the isothermal-isobaric (NPT) ensemble to stabilize pressure and density. Finally, a 100 ns production simulation was executed in the NPT ensemble using a 2 fs integration time step, with trajectory data recorded every 40 ps for subsequent analysis.

2.4. *Preparation of Bai-Fe(III) ICP@Pro NCPs*

Bai-Fe(III) ICP nanocomposites (Bai-Fe(III) ICP NPs) loaded with propofol (Pro) and baicalin (Bai) were prepared via a self-assembly method. Briefly, 10 mg of $FeCl_3$, 20 mg baicalin, and 200 mg benzoic acid were dissolved in 20 ml N,N-dimethylformamide to obtain a homogeneous solution, which was then transferred into a three-neck round-bottom flask equipped with a temperature probe. The solution was stirred magnetically at medium speed and heated to 95 ± 2 °C in an oil bath, maintaining this temperature for 4 h to facilitate porous coordination between the metal ions and ligands. Upon completion, the product was collected by centrifugation, thoroughly washed, and dried to yield Bai-Fe(III) ICP NPs. These nanoparticles were then suspended in an aqueous solution containing 0.2% (w/w) Pluronic F-127 (F127), followed by the addition of 50 µl propofol. The mixture was stirred at 1800 rpm for 12 h to maximize propofol loading and ensure uniform dispersion. The resulting Bai-Fe(III) ICP@Pro NCPs were dialyzed using a 3,500 KDa MWCO dialysis bag for 24 h, with water changes every 4–6 h to remove free drug and residual impurities. Finally, the nanoparticle suspension underwent additional purification steps, including dialysis, ultrafiltration, centrifugation, and lyophilization, to obtain highly pure nanocomposites suitable for subsequent experiments and long-term storage.

2.5. *Characteristics of Bai-Fe(III) ICP@Pro NCPs*

The hydrodynamic diameter and zeta (ζ) potential of Bai-Fe(III) ICP@Pro NCPs were determined using a Malvern Zetasizer Nano ZS90 (Malvern Instruments Ltd., UK). Morphology and particle size were examined by high-resolution transmission electron microscopy (HR-TEM, JEM-F200, JEOL Ltd., Japan). The chemical composition was analyzed using UV–Vis absorption spectroscopy (PG Instruments, China) and Fourier-transform IR (FTIR) spectroscopy (Ettlingen, Germany). Drug quantification within the nanocomposites was performed by high-performance liquid chromatography (HPLC, Agilent, CA, USA) as described in Table S4. The mobile phase comprised acetonitrile (A) and 0.5% phosphoric acid aqueous solution (B), applied in gradient elution mode. Nitrogen adsorption-desorption isotherms were recorded at −196°C using a Micromeritics Tristar 3020, and pore size distribution was calculated via the Barrett-Joyner-Halenda method. X-ray photoelectron spectroscopy (XPS) was carried out using an ESCALAB Xi+ system (Thermo Fisher, USA), while crystal structure was characterized by X-ray diffraction (XRD):

$$\text{Drug loading content (\%)} = \frac{\text{Total mass of the drug in nanocomposites}}{\text{Tolal mass of the nanocomposites}} \times 100\%$$

(Note: mass in mg, volume in ml).

2.6. *FUS parameters and in vivo BBB opening*

The FUS apparatus used in this study comprised three primary components: a waveform signal generator (Model DG1062, RIGOL, China), a radiofrequency power amplifier (Model AG1016, Tektronix, USA), and a precision-engineered single-element transducer (ndtXducer®, Northborough, USA). The transducer was configured to operate at a center frequency of 1 MHz with an effective focal length of approximately 5 cm. Acoustic parameters for *in vivo* BBB disruption were adapted from previously validated protocols, with slight modifications to meet the experimental requirements. C57BL/6 mice

(12–16 g) were anesthetized with 1% sodium pentobarbital, immobilized in a stereotaxic apparatus, and exposed to FUS at a central frequency of 1 MHz, a pulse repetition rate of 1 Hz, a duty cycle of 10%, and an exposure duration of 1 min. For safety evaluation, subsets of animals were euthanized immediately or 2 h post-FUS, and brains were harvested, fixed in 4% paraformaldehyde in PBS, and processed for histological assessment using hematoxylin and eosin (H&E) and Nissl (methylene blue) staining. Brain sections were examined using NDP. View 2 software on the 3D HISTECH imaging platform (Hungary). To assess BBB permeability, C57BL/6 male mice (12–16 g, $n = 3$ per group) were anesthetized and positioned in the stereotaxic frame, after which varying volumes of SonoVue MBs were injected intravenously via the tail vein, followed by FUS exposure at different acoustic intensities. Immediately thereafter, 60 μl of 2% Evans Blue (EB) dye was administered intravenously. Mice were euthanized at 0 min, 30 min, 60 min, 120 min and 180 min post-treatment, and harvested brains were imaged and analyzed to evaluate BBB disruption and dye extravasation.

2.7. *In vitro cytotoxicity test*

The CCK-8 assay was conducted to assess the *in vitro* cytotoxicity of different treatment formulations. HT22 neuronal cells were seeded into 96-well plates and cultured in high-glucose DMEM supplemented with 10% fetal bovine serum and 1% penicillin-streptomycin. Cells were then treated with various formulations, including propofol, baicalin, a combination of propofol and baicalin (Mix, Pro+Bai), and Bai-Fe(III) ICP@Pro NCPs, for incubation periods of 4 h and 12 h. Following the incubation, 100 μl freshly prepared culture medium and 10 μl CCK-8 reagent were added to each well. The plate was then returned to the incubator for an additional 4 h incubation to allow the reaction to proceed. After the colorimetric reaction was completed, the absorbance (OD value) of each well was measured at 450 nm using a microplate reader.

2.8. *In vivo fluorescent imaging*

To investigate the brain distribution of propofol, *in vivo* fluorescence imaging was conducted using the IVIS Lumina III imaging system (Caliper Life Sciences, Massachusetts, USA), equipped with IR780 fluorescence and X-ray capabilities. Twenty-four depilated C57BL/6 mice were anesthetized with isoflurane and randomly assigned to two groups: one group received intravenous MBs followed by FUS treatment, while the other served as a control. Dorsal hair removal was performed using electric clippers and depilatory cream (Veet), followed by thorough rinsing with sterile saline. About 2 h after preparation, mice were administered 0.15 ml of either free IR780 or Bai-Fe(III) ICP@IR780 NCPs (IR780 dose: 0.25 mg/kg) via tail vein injection. Fluorescence signals were acquired at predetermined time intervals using the Xenogen IVIS® Lumina system. For *ex vivo* biodistribution analysis, mice were euthanized 4 h post-injection, and major organs, including the brain, heart, liver, spleen, lungs, and kidneys, were harvested, rinsed with saline, and imaged under identical fluorescence parameters to evaluate organ-specific accumulation.

2.9. *TI determination*

TI, a key parameter for assessing drug safety and efficacy, was determined as the ratio of the median lethal dose (LD_{50}) to the median ED_{50}. A preliminary dose-ranging study was conducted in healthy C57BL/6 mice (12–16 g, $n = 10$ per group) to establish an appropriate dosing range for formal evaluation. In the pre-test, various drug concentrations were administered, and anesthetic efficacy was assessed based on the righting reflex recovery time: recovery within 20 s was classified as ineffective (-), whereas recovery exceeding 20 s was considered effective anesthesia (+). Mortality within 24 h was recorded as a lethal outcome (+), while survival was considered non-lethal (-). For the formal TI assessment, approximately 50 mice were randomly assigned to five groups, each receiving a different drug concentration determined from the pre-test results. Righting reflex responses and survival outcomes were documented, and ED_{50} and LD_{50} values were calculated using the Bliss method. The TI was then computed as the ratio of LD_{50} to ED_{50} (Tables S5 and S6).

2.10. *Physiological indexes in anesthetized mice*

Healthy C57BL/6 mice (balanced for sex, 12–16 g) were randomly assigned to four groups, Free, MIX, Bai-Fe(III) ICP@Pro NCPs, and Bai-Fe(III) ICP@Pro NCPs + US, with five mice per group. Each group received its respective formulation via tail vein injection, and in the Bai-Fe(III) ICP@Pro NCPs + US group, administration followed US-MBs treatment. The experimental timing commenced when the mouse's righting reflex disappeared and continued until its restoration, with anesthesia durations of at least 20 s considered effective. Following the initial experiment, anesthesia duration for each mouse was recorded, and group averages were calculated. Mice were then placed in a temperature-controlled container (37 °C) for acclimatization, after which their tails were exposed and secured using a fixed device. A pressure cuff from a blood pressure monitor was positioned near the tail base, and once the mice were settled, each group received an equal anesthesia dose ($1.5 \times ED_{50}$). Blood pressure and heart rate were measured at five predefined time points using a non-invasive sphygmomanometer (Mouse BP-2010A, Softron Biotech Co., Ltd., Beijing, China), with the mean value at each time point calculated for every group. Anesthesia duration was defined as the time from disappearance of the righting reflex until its reappearance.

2.11. *Neurotoxicity evaluation of drug formulations*

To evaluate potential neurotoxicity, 3-week-old C57BL/6 juvenile mice ($n = 40$) were randomly assigned to four groups ($n = 10$ per group): Control, Propofol, Bai-Fe(III) ICP@Pro NCPs, and Bai-Fe(III) ICP@Pro NCPs + US. The control group received no treatment, while the experimental

groups underwent anesthesia with either propofol or the nanoparticle formulations, with one group additionally receiving transcranial US in combination with nanocomposite administration. Anesthesia was induced by intraperitoneal injection of propofol at a dose of 100 mg/kg, administered at a rate of 0.1 ml/min, followed by hourly maintenance doses of 50 mg/kg for 6 h on two consecutive days, with onset confirmed by the disappearance of the righting reflex. Throughout anesthesia, mice were maintained in a temperature-controlled incubator with 100% oxygen to ensure stable respiration and homeostasis. Upon full recovery, animals were returned to their cages for a 5d observation and feeding period. Subsequently, four mice from each group were randomly selected for brain histological analysis; brains were collected, fixed, and subjected to H&E staining as well as Nissl staining with tar violet solution to assess potential neurodegenerative changes (Fig. S3). The remaining six mice per group underwent behavioral testing to evaluate post-anesthetic cognitive and motor function.

2.12. *Behavioral experiment*

All behavioral assessments were performed in a darkened environment to align with the mice's natural circadian activity. Prior to testing, mice underwent a three-day acclimatization period involving daily handling and systematic desensitization to minimize anxiety and emotional variability, thereby improving the reliability of behavioral data. Behavioral data were recorded and analyzed using SMART 3.0 (Panlab, Spain), a specialized behavioral tracking software.

2.12.1. *Open field test (OFT)*

OFT was used to assess spontaneous locomotor activity and exploratory behavior. The test apparatus consisted of a square box measuring 50 × 50 × 40 cm^3 (L × W × H), equipped with an overhead IR night-vision camera to record movements. Mice were acclimated to the testing room for 1 h prior to the experiment under low-light and low-noise conditions to reduce stress and ensure reliable behavioral measurements (Fig. S7A).

During testing, each mouse was placed in the open field facing the wall and allowed to explore freely for 5 min. Recorded parameters included total movement distance, average speed, time spent in the central zone, and distance traveled within the central zone. After each trial, mice were returned to their home cages, and the arena was thoroughly cleaned with 75% ethanol to remove olfactory cues.

$$\text{Ratio of distance to center area (\%)} = \frac{\text{Movement distance in the central area}}{\text{Total movement distance}} \times 100\%$$

(Note: percentage of total distance (%) ± SD).

2.12.2. *Novel object recognition test (NORT)*

The NORT was performed to evaluate learning and memory by exploiting the animal's natural preference for novel objects. The test used the same open field arena (50 × 50 × 40 cm^3) and consisted of two phases: a training phase and a testing phase (Fig. S7C).

During the training phase, two identical objects (A and B) were positioned approximately 5 cm from the arena walls, allowing mice to explore freely. Each mouse was placed equidistant from the two objects with its back facing them and permitted to explore for 5 min. Exploration time was defined as the duration spent within 2 cm of each object, excluding periods of stationary proximity).

Following the training phase, both the objects and the arena were thoroughly cleaned with 75.0% ethanol. About 1 h later, during the testing phase, object B was replaced with a novel object C, differing in shape and color. Mice were reintroduced into the arena and allowed to explore for 5 min. Recognition Index (RI) was then calculated as follows:

$$\text{Recognition Index (\%)} = \frac{\text{Time exploring new object}}{\text{Time exploring new object} + \text{Time exploring familiar object}} \times 100\%$$

A higher RI reflects improved recognition memory. After each trial, all objects and the arena were thoroughly disinfected to prevent odor-based interference.

2.12.3. *Y-Maze test*

Y-maze test was employed to evaluate short-term spatial memory and spontaneous alternation behavior, indicative of hippocampal and prefrontal cortex function. The maze consisted of three arms, each measuring 30 cm in length, 10 cm in width, and 15 cm in height, arranged at 120° angles. Mice were acclimated to the testing room for 1 h prior to the experiment (Fig. S7B).

Each mouse was placed at the end of one arm and allowed to explore the Y-maze freely for 5 min. An arm entry was recorded when all four paws entered an arm. A "rotation" was defined as three consecutive entries into three different arms without repetition. The Alternation Score was calculated using the following formula:

$$\text{Alternation Score (\%)} = \frac{\text{Number of alternations}}{\text{Total Number of entries} - 2} \times 100\%$$

After each session, all arms were wiped with 75% ethanol to remove residual odors.

2.13. *Statistical analysis*

All data are presented as the mean ± standard deviation (SD) from a minimum of three independent experiments. Statistical comparisons between two groups were performed using the unpaired Student's t-test. For comparisons involving multiple groups, one-way analysis of variance (ANOVA) was applied, followed by the least significant difference (LSD) post hoc test where appropriate. A P-value <0.05 ($P < 0.05$) was considered statistically significant.

3. Results and discussions

3.1. *Design and preparation*

Although general anesthetics are widely used in clinical practice, their extensive application is frequently associated with significant side effects. To overcome these limitations, we developed a porous nanostructure based on baicalin, a natural flavonoid with neuroprotective properties, for high-capacity encapsulation and delivery of propofol. The hydroxyl groups present in both baicalin and propofol facilitate strong intermolecular interactions, enabling efficient encapsulation of propofol within the baicalin matrix as well as adsorption onto the nanoparticle surface. This dual localization markedly enhances propofol-loading efficiency. Upon FUS stimulation, the nanocomposite effectively crosses the BBB, delivering rapid anesthetic effects while concurrently providing sustained neuroprotection through gradual baicalin release.

To investigate the potential for high drug loading with minimal carrier usage, MD simulations were conducted. As illustrated in Fig. 1A, randomly distributed propofol (blue) and baicalin (red) molecules were placed in a cubic simulation box ($5 \times 5 \times 5$ nm^3) under periodic boundary conditions. Over a 100-ns MD simulation, stable intermolecular hydrogen

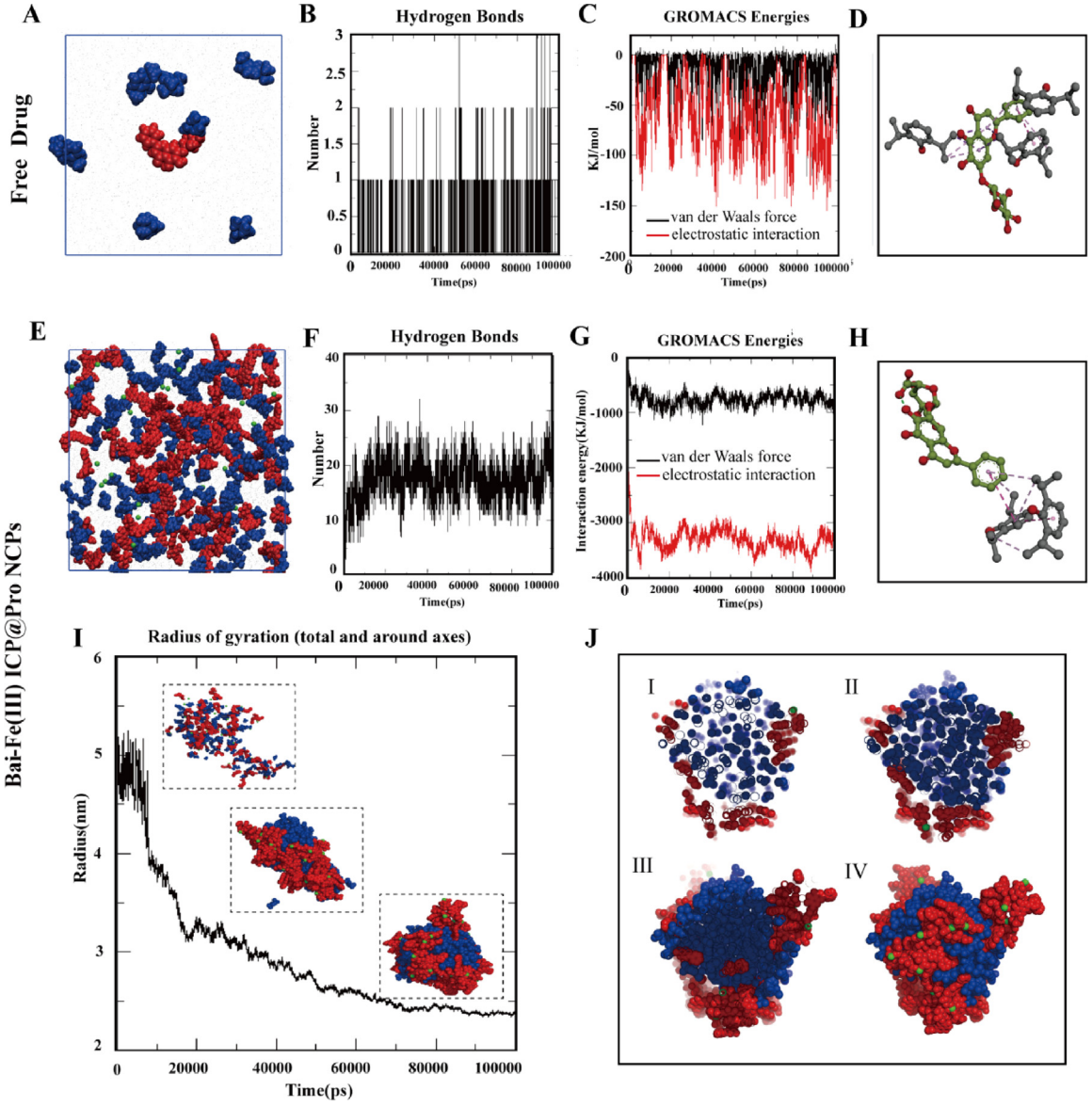


Fig. 1 – Analysis of interactions between free drugs and the formation of Bai-Fe(III) ICP@Pro NCPs. The system for free baicalin (red) and propofol (blue) was first established (A), followed by investigation of hydrogen bond formation (B), van der Waals forces, and electrostatic interactions during the kinetic simulation process (C). (D) Detailed direct interactions between baicalin and propofol. (E-H) Depict the construction of Bai-Fe(III) ICP@Pro NCPs, with analyses of hydrogen bonds, van der Waals forces, electrostatic interactions, and detailed mutual molecular interactions. (I) Simulation progresses, the radius of gyration gradually decreases and stabilizes around 2.5 nm. (J) Overall formation process of Bai-Fe(III) ICP@Pro NCPs.

bonds formed between the molecules (Fig. 1B and 1C). Notably, van der Waals interactions were markedly stronger than electrostatic forces, indicating that the system is predominantly stabilized by non-covalent, hydrophobic interactions. The calculated binding free energy between baicalin and propofol was −12 kcal/mol, with van der Waals forces contributing −16 kcal/mol and electrostatic interactions contributing −3 kcal/mol (Table S1). Fig. 1D further demonstrates direct molecular contacts between the two compounds, highlighting extensive π-π stacking and hydrophobic interactions (dashed lines) that enhance structural stability.

To simulate nanocomposite formation, an expanded system (10 × 10 × 10 nm^3) was modeled containing baicalin (red), propofol (blue), and Fe^{3+} ions (green) under periodic boundary conditions. Over the 100 ns simulation, approximately 20 hydrogen bonds formed between baicalin and propofol, stabilizing after 50 ns (Fig. 1F) and playing a crucial role in maintaining nanocomposite integrity. The interaction energies were predominantly governed by van der Waals forces (−934 kcal/mol), with a total binding free energy of −476 kcal/mol (Fig. 1G, Table S2), accounting for 73% of free energy contribution, greatly higher than that of baicalin and propofol of molecular interaction and confirming robust molecular cohesion. Fig. 1H illustrates that the interaction mechanisms within the nanocomposite closely mirror those observed in free molecules, primarily driven by hydrophobic contacts and π-π stacking. As the simulation progressed, the radius of gyration decreased steadily (Fig. 1I and 1J), indicating that baicalin encapsulated propofol within an internal cavity, while excess propofol aggregated on the particle surface, forming a dense core-shell nanostructure. These results validate the feasibility of constructing highly loaded, carrier-free nanocomposites, and highlight the dual therapeutic function of baicalin, facilitating propofol loading while providing intrinsic neuroprotection, potentially mitigating adverse effects associated with conventional anesthetics.

3.2. *Characterization of Bai-Fe(III) ICP@Pro NCPs*

We developed a novel nanocomposite system, Bai-Fe(III) ICP@Pro NCPs, based on an ICP framework for encapsulating the general anesthetic propofol. In this system, baicalin self-assembled into a porous nanostructure and coordinated with Fe^{3+} ions to form the ICP matrix. Propofol was loaded both within the internal cavities and adsorbed onto the nanoparticle surface via hydrogen bonding and other intermolecular interactions, producing stable dual-drug nanocomposites. TEM images (Fig. 2A) revealed that the Bai-Fe(III) ICP@Pro NCPs exhibited uniform spherical morphology with an average diameter of 92.3 ± 10.2 nm. A high-contrast, compact core corresponding to the ICP structure was observed, surrounded by a low-contrast peripheral layer attributed to surface-adsorbed propofol. During Bai-Fe(III) ICP NP preparation, particle size increased progressively with extended reaction time (Fig. 2B). A 5 h reaction yielded Bai-Fe(III) ICP NPs with a mean particle size of approximately 80 nm, which were selected as the nanocarrier matrix for subsequent propofol loading.

Following propofol encapsulation, the Bai-Fe(III) ICP@Pro NCPs exhibited a hydrated particle diameter of 123.0 ± 11.5 nm (Fig. 2C-2E) and a positively charged surface, which is favorable for biological interactions and systemic circulation. The nanocomposites demonstrated excellent colloidal stability, with negligible changes in hydrodynamic diameter over a 90-d storage period. UV–Vis spectroscopy was employed to investigate baicalin-Fe^{3+} coordination (Fig. 2F); the characteristic baicalin absorption peaks at ~250 nm and ~350 nm disappeared upon coordination, indicating coordination-induced electronic transitions. Acid hydrolysis restored these peaks, confirming that the ICP nanostructure is chemically stable yet responsive to environmental conditions. FTIR spectroscopy further revealed molecular interactions within the nanocomposites (Fig. 2G). The broad -OH stretching vibration of free baicalin at 3411 cm^{-1} shifted to 3467 cm^{-1} in the nanocomposite, reflecting hydrogen bonding and coordination with Fe^{3+}, while carboxyl peaks at 1774 cm^{-1} and 1755 cm^{-1} vanished, indicating their direct involvement in complexation. The -OH stretching vibration of free propofol at 3574 cm^{-1} was broadened in the final formulation, suggesting strong hydrogen bonding and potential coordination interactions [21]. XPS confirmed successful Fe^{3+} coordination (Fig. 2I), with survey spectra showing C, O, and Fe elements. High-resolution Fe 2p spectra (Fig. S1) revealed peaks at 710.80 eV and 725.16 eV, deconvoluted into Fe $2p_{3/2}$ (709.10 eV), Fe $2p_{3/2}$ satellite (711.58 eV), Fe $2p_{1/2}$ (721.90 eV), and Fe $2p_{1/2}$ satellite (724.20 eV), consistent with electron donation to Fe^{3+}. Additionally, O 1 s binding energies in Bai-Fe(III) ICP@Pro NCPs (530.72 eV and 533.00 eV) were higher than in free baicalin (529.30 eV and 531.20 eV), further supporting coordination (Table S3). XRD patterns (Fig. 2H) indicated an amorphous Fe(III)-Bai ICP structure, confirming ICP formation without long-range crystallinity. Nitrogen adsorption-desorption isotherms (Fig. 2J) demonstrated a porous architecture with a specific surface area of 81.85 m^2/g, a pore volume of 0.322 cm^3/g, and an average pore diameter of 5.1 ± 0.2 nm, suitable for propofol loading and diffusion. HPLC quantified propofol and baicalin content, with detection at 278 nm and retention times of 30.65 min for propofol and 19.54 min for baicalin (Fig. S2). Analysis revealed a propofol-to-baicalin mass ratio of 6:1, corresponding to a high propofol loading efficiency of approximately 62%, confirming the strong encapsulation capacity of the nanocomposites.

3.3. *Conditions of opening BBB by US-MBs*

Effective, transient, and safe opening of the BBB is crucial for achieving rapid and large-scale drug delivery into the brain. FUS-MBs has emerged as a promising non-invasive strategy for transient BBB disruption, facilitating enhanced intracerebral drug delivery [35,36]. To determine the optimal parameters for BBB opening using this approach, EB dye was employed as a tracer for BBB permeability in experiments conducted on C57BL/6 male mice (12–16 g). Mice were administered varying volumes of MBs and subsequently treated with FUS using the ndtXducer® system. FUS irradiation was applied for 1 min with a center frequency of 1 MHz, a pulse repetition frequency of 1 Hz, and a 10% duty

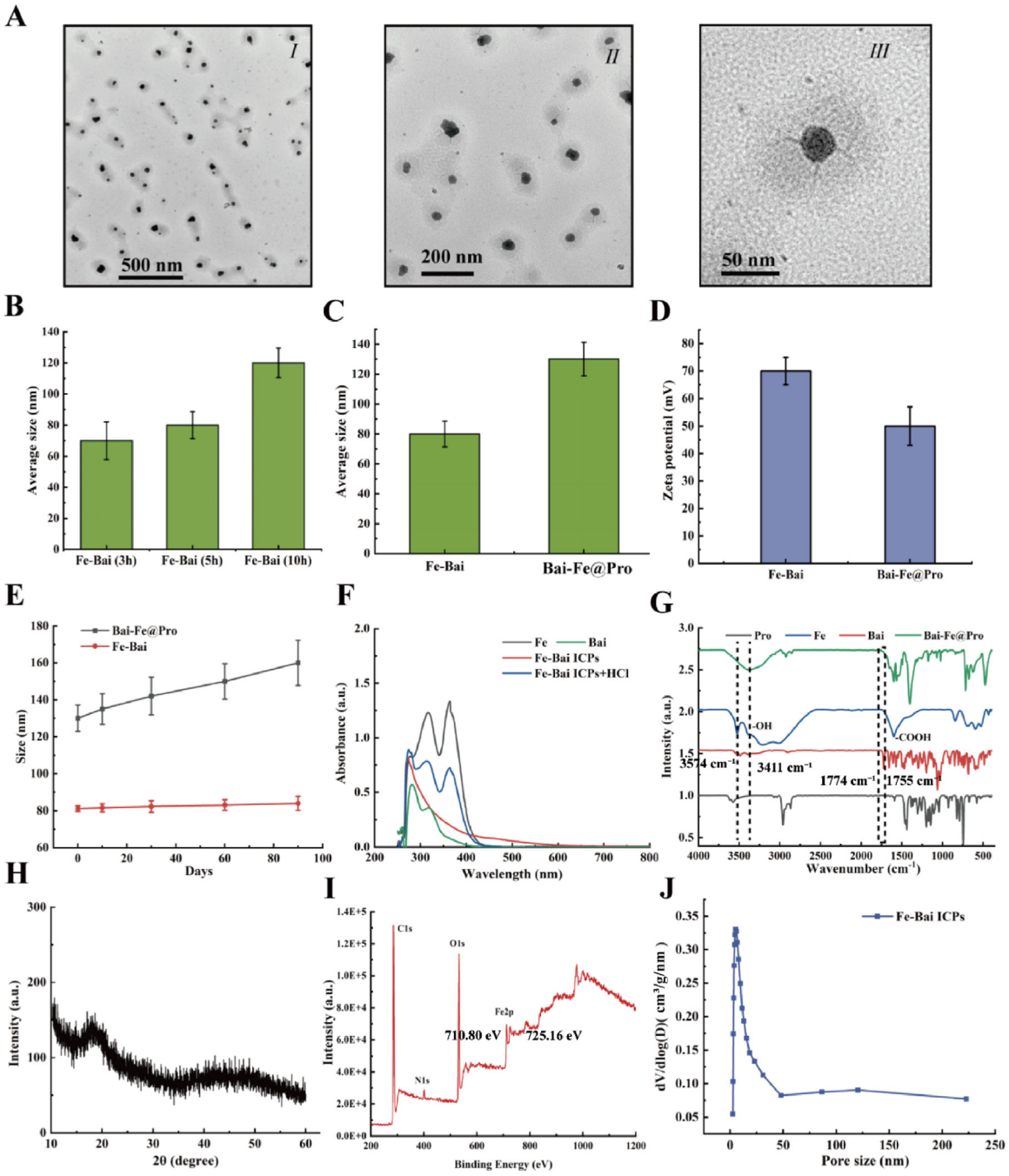


Fig. 2 – Characteristics of Bai-Fe(III) ICP@Pro NCPs were systematically investigated. (A) TEM images of Bai-Fe(III) ICP@Pro NCPs captured at different magnifications (I: ×20k; II: ×50k; III : ×200k), illustrating their morphology and structural features. (B) Average particle size of Bai-Fe(III) ICP NPs evaluated under varying reaction durations. (C) Average particle size of Bai-Fe(III) ICP@Pro NCPs was determined after a 5 h reaction period. (D) Zeta potential measurements provided insights into the surface charge properties of the nanocomposites. (E) Stability of the nanocomposites was assessed at −4 °C, confirming their structural integrity under low-temperature conditions. (F) Ultraviolet (UV) spectra and (G) IR spectra analyzed to evaluate the optical and chemical properties of the samples, respectively. (H) XRD results, revealing the crystallographic characteristics of Bai-Fe(III) ICP@Pro NCPs. (I) XPS full spectrum, providing detailed surface elemental composition. (J) Pore size distributions were measured, confirming the textural properties of Bai-Fe(III) ICP@Pro NCPs.

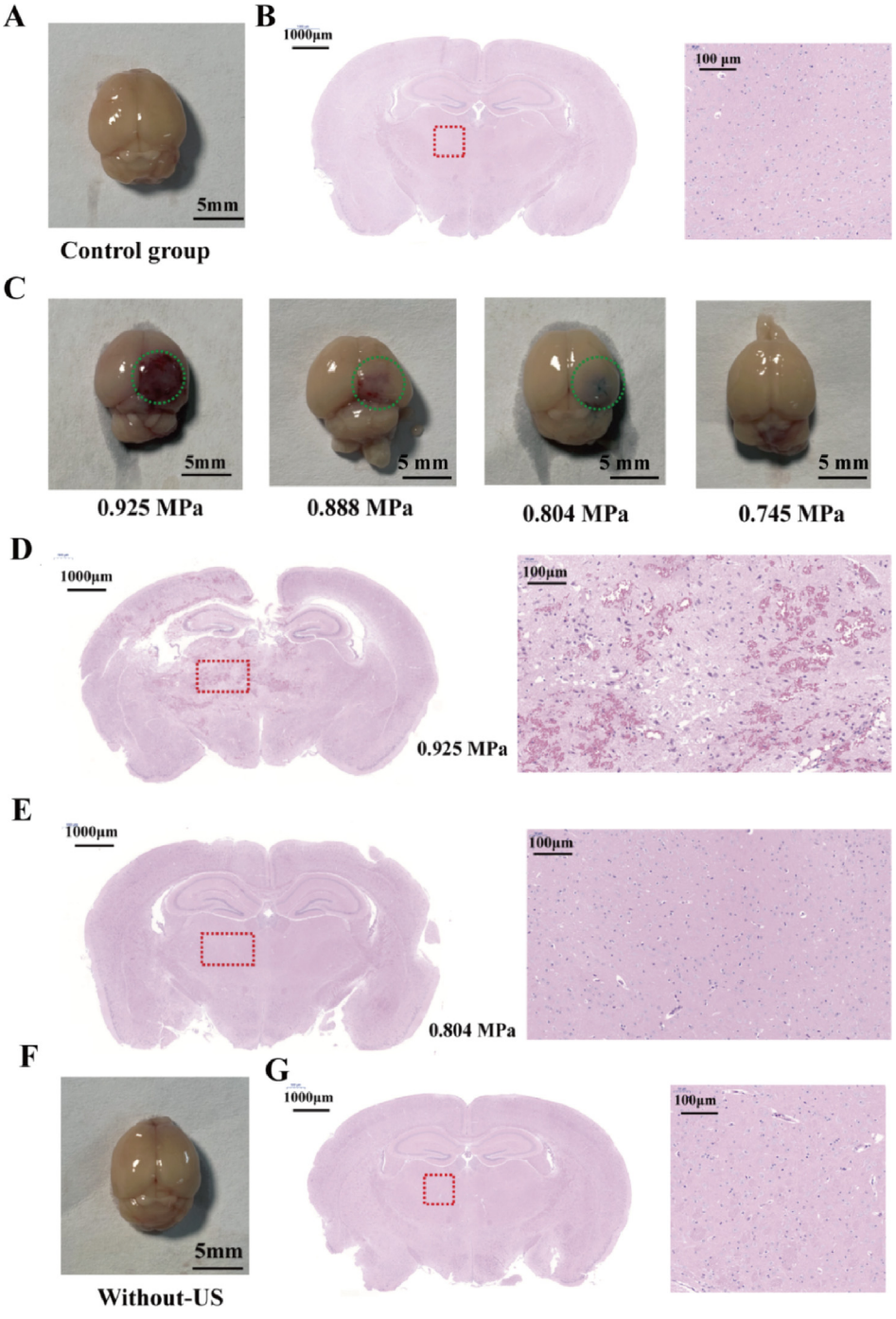


Fig. 3 – Variation in the degree of BBB opening with sound pressure following US-MBs treatment is shown. (A) Representative photographs of untreated mouse brains and (B) their corresponding H&E-stained sections are presented. (C) Quantitative results of BBB opening at different sound pressures are shown, along with (D-E) representative H&E-stained sections (scale bar: 1000 μm). (F) BBB opening at 0.804 MPa assessed with EB dye and (G) the corresponding H&E-stained sections are illustrated. Experimental parameters included a transducer center frequency of 1 MHz, a pulse repetition rate of 1 Hz, a 10% duty cycle, an ultrasonic duration of 1 min, and a microbubble dosage of 100 μl.

cycle. The extent of BBB opening was then assessed based on EB extravasation, providing a quantitative measure of BBB permeability.

Following treatment, mice were intravenously injected with a 2% EB solution. As shown in Fig. 3A and 3B, brain tissues from untreated control mice exhibited no EB signal and displayed normal histological features in H&E staining, confirming BBB integrity and the absence of tissue injury. In contrast, mice exposed to higher US pressures (0.925 MPa and 0.888 MPa) showed evident brain damage, including cerebral

hemorrhage and structural disorganization on histological sections (Fig. 3C-3E). At 0.804 MPa, clear EB penetration into the brain parenchyma was observed without any detectable tissue injury in H&E-stained sections, indicating successful and safe BBB opening. However, when the sound pressure was reduced below 0.745 MPa, EB failed to accumulate in the brain, suggesting that the BBB remained intact under these conditions (Fig. 3F-3G). Additionally, mice that did not receive US exposure exhibited no EB signal in the brain, further confirming that the BBB remained intact in the absence of US-MBs.

Based on these findings, a sound pressure of 0.804 MPa with 30% acoustic gain was selected for all subsequent experiments. To further optimize microbubble dosage, the relationship between microbubble volume and BBB opening was investigated. As shown in Fig. 3, EB extravasation increased with the administered microbubble volume, with little to no BBB opening observed below 40 μl. Effective BBB disruption was achieved only when the microbubble volume exceeded 60 μl. Histological analysis of brain tissues from mice treated with 100 μl MBs revealed no evidence of hemorrhage or structural damage, confirming the safety of the selected conditions. Collectively, these results demonstrate that FUS-mediated BBB opening is both pressure- and dose-dependent, with a sound pressure of 0.804 MPa combined with ≥60 μl MBs achieving safe, effective, and reversible BBB opening by disrupting tight junctions between endothelial cells (Fig. S4). These optimized parameters were subsequently employed for Bai-Fe(III) ICP@Pro NCPs experiments in this study.

3.4. *In vivo imaging*

The reversible opening of BBB mediated by US-MBs significantly enhances drug delivery efficiency to the brain. To directly visualize this process, the hydrophobic fluorescent dye IR780 was employed as a model drug to track its distribution following FUS-MBs treatment. Healthy male C57 BL/6 mice (12–16 g) were randomly and equally divided into two groups: one group received pretreatment with US-MBs, while the other did not. Both groups were subsequently injected with either free IR780 or Bai-Fe(III) ICP@IR780 NCPs, and the distribution of IR780 was observed approximately 2 h post-injection. Accumulation of IR780 in the brain over time was monitored using the IVIS Fluorescence Imaging System (Caliper Life Sciences, Massachusetts, USA), with results shown in Fig. 4A. Significant fluorescence signals were detected in all ultrasonically treated mice compared to untreated mice, and the fluorescence intensity increased over time. At 4 h post-treatment, fluorescence in the US + Free IR780 group was 1.89 times higher than in the Free IR780 group, while fluorescence in the US + Bai-Fe(III) ICP@IR780 NCPs group was 3.10 times higher. Under identical conditions, FUS-MBs-treated mice exhibited more intense fluorescence and earlier signal detection than untreated mice. To identify the brain regions contributing to the fluorescence signals, ex vivo fluorescence images of the brain and other organs were acquired 4 h post-injection (Fig. 4B). Quantification of fluorescence intensity (Fig. 4B) indicated that brain uptake of Free IR780 increased 1.85-fold following US treatment, whereas Bai-Fe(III) ICP@IR780 NCPs exhibited a 2.25-fold increase in brain fluorescence (Fig. S5). These results demonstrate that the US-MBs approach facilitates efficient drug delivery to the brain with minimal accumulation in other organs (Fig. S6), thereby reducing potential toxicity associated with anesthetics.

In summary, we propose that targeting brain delivery using US-MBs can significantly enhance the delivery of anesthetics and other drugs to the brain while reducing their accumulation in other organs. This approach not only facilitates the synergistic action of the anesthetics but also increases the effect by 3.472-fold compared with the free drug, allowing for a reduction in their total dosage, thereby minimizing toxic and side effects on various organs. Furthermore, neuroprotective drugs can be efficiently delivered to the brain, mitigating potential anesthetic-induced damage and achieving the dual objectives of reducing toxicity and enhancing therapeutic efficacy. In summary, ultrasound enhances blood-brain barrier permeability, thereby amplifying propofol delivery and augmenting the neuroprotective effects of baicalin.

3.5. *Cytotoxicity of Bai-Fe(III) ICP@Pro NCPs*

The cytotoxicity of different drug formulations was assessed using a CCK-8 assay in HT22 hippocampal neuronal cells, revealing that Bai-Fe(III) ICP@Pro NCPs significantly reduced the neurotoxicity associated with free propofol. As shown in Fig. 5A, after 4 h of treatment, free propofol induced a concentration-dependent decline in cell viability, decreasing from 98% ± 2% to 55% ± 3% at 60 μg/ml, whereas baicalin alone exhibited negligible toxicity, with viability remaining above 90% at the same concentration. A mixture of free propofol and baicalin (MIX group, 1:6 mass ratio) provided partial protection, maintaining approximately 70% viability, yet this was notably less effective than Bai-Fe(III) ICP@Pro NCPs, which preserved over 80% viability under identical conditions. Upon extending treatment to 12 h (Fig. 5B), the neurotoxicity of free propofol became more severe, reducing cell survival to 30% ± 5% at 60 μg/ml, which was twice as high as the cell mortality observed at 4 h. Baicalin-treated cells remained unaffected, with survival exceeding 95%. The MIX group declined further to about 50%, indicating limited long-term protection by free baicalin co-administration, whereas Bai-Fe(III) ICP@Pro NCPs-treated cells maintained over 70% viability, demonstrating sustained cytoprotection. Live/dead cell staining corroborated these findings: after 4 h, free propofol caused a notable reduction in viable cells and altered morphology (Fig. 5C and 5E), whereas Bai-Fe(III) ICP@Pro NCPs retained more viable cells with relatively intact morphology. Following 12 h of exposure (Fig. 5D and 5F), substantial cell death was observed in the free propofol group, while cells treated with Bai-Fe(III) ICP@Pro NCPs showed only a slight decline in viability. Collectively, these results indicate that Bai-Fe(III) ICP@Pro NCPs effectively mitigate

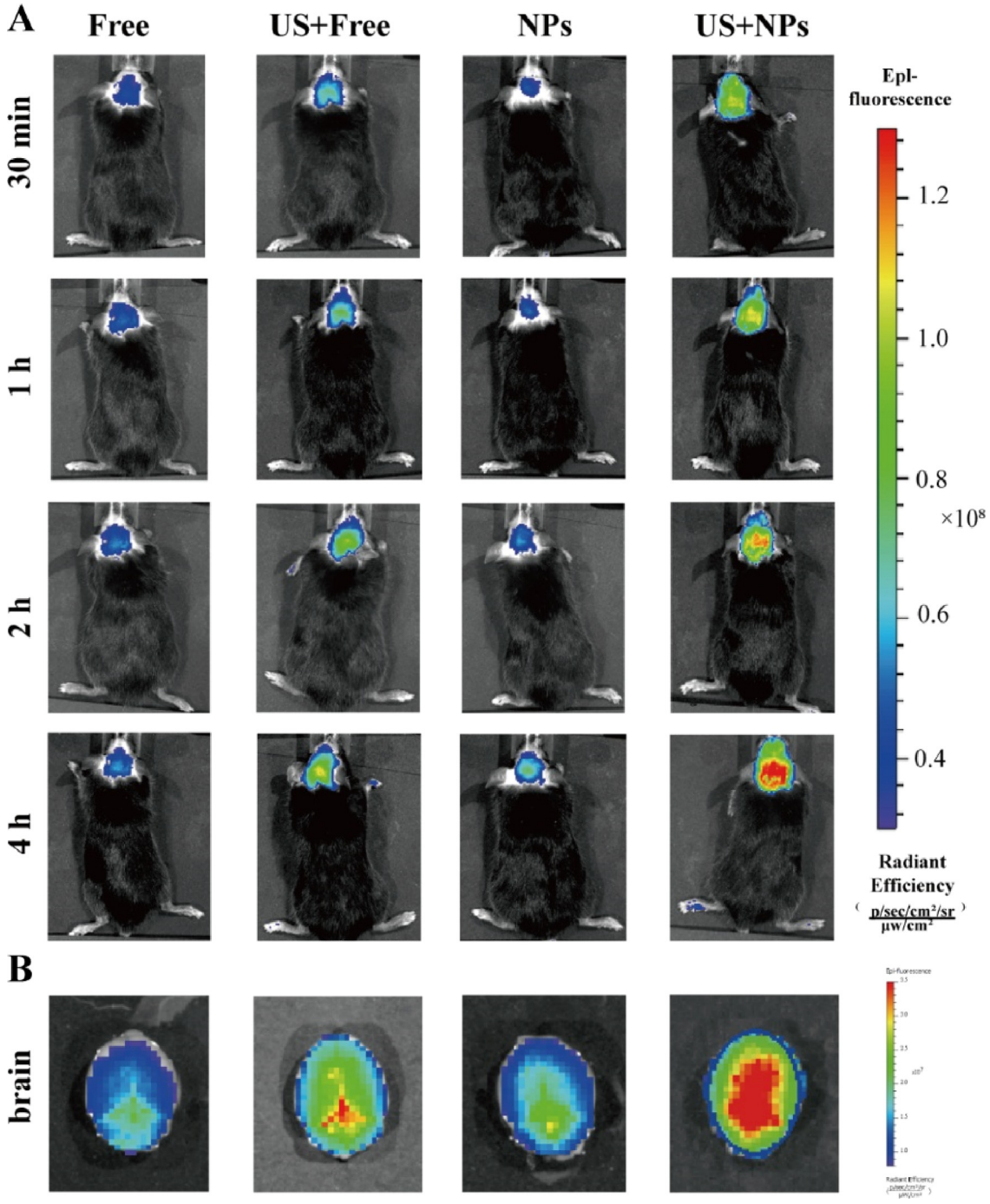


Fig. 4 – *In vivo* fluorescence imaging. (A) Real-time fluorescence imaging of mice following different treatments and (B) *ex vivo* fluorescence images of brains post-injection are shown. Mice were randomly injected via the tail vein with 0.1 ml of either free IR780 or Bai-Fe(III) ICP@IR780 NPs, with the US group receiving injections 2 h after US irradiation (IR780: 2.5 mg/kg; $n = 3$). The excitation and emission wavelengths for IR780 imaging were 780 nm and 810 nm, respectively. Fluorescence intensity was quantified in arbitrary units (± SD, $P < 0.01$) at 4 h post-injection, corresponding to the peak of the pharmacokinetic profile.

propofol-induced neurotoxicity, prolong neuronal survival, and maintain cellular integrity over extended periods, highlighting the formulation's protective and time-stable advantages as a promising candidate for safer anesthetic delivery.

3.6. *Anesthetic effect of Bai-Fe(III) ICP@Pro NCPs*

Anesthesia monitoring is essential for evaluating anesthetic efficacy and safety, as it allows continuous tracking of physiological parameters and real-time assessment of

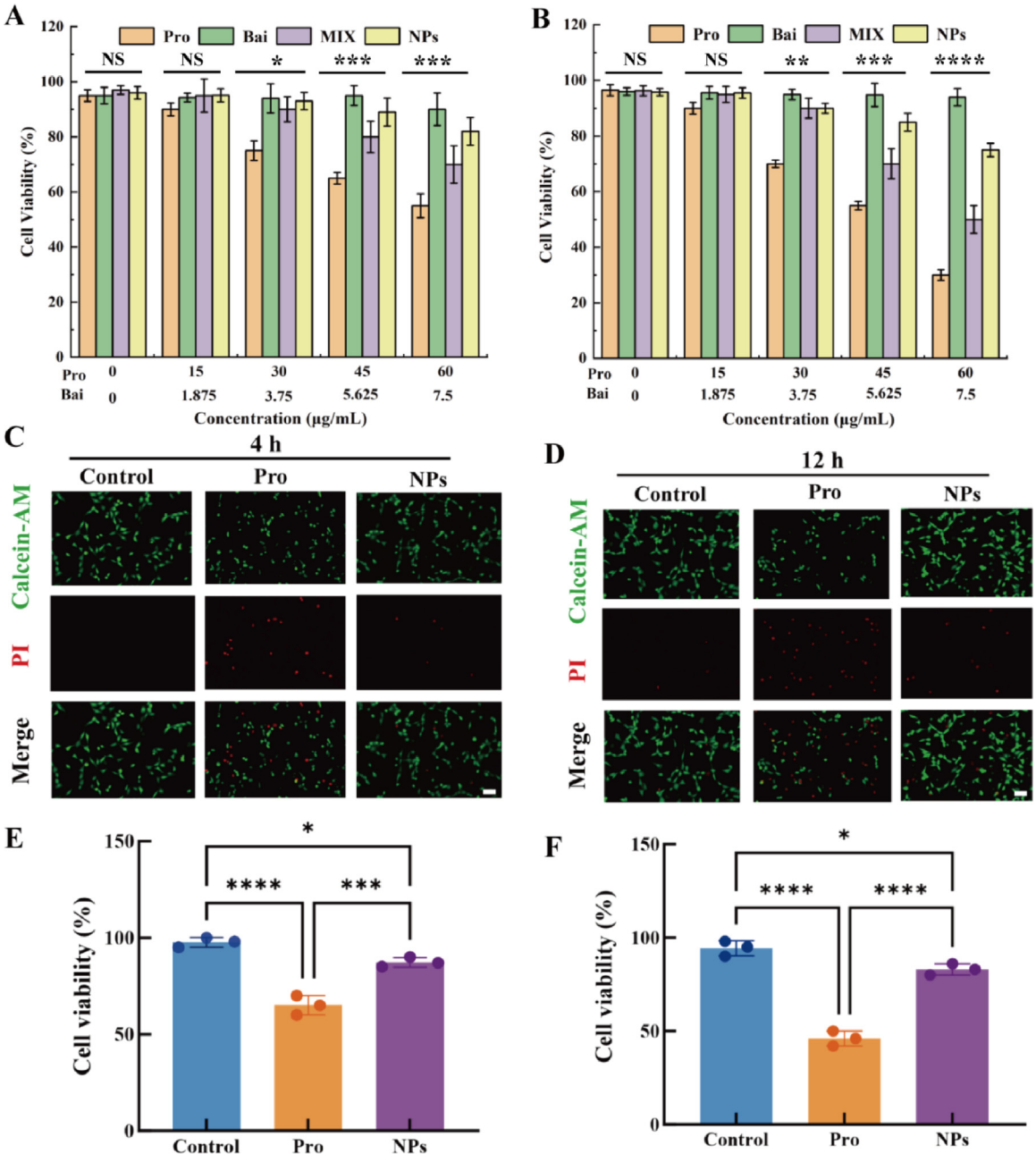


Fig. 5 – (A,B) *In vitro* cytotoxicity test results. Cell viability of HT22 cells treated with varying concentrations of propofol, baicalin, MIX, and Bai-Fe(III) ICP@Pro NCPs is shown for (A) 4 h and (B) 12 h (The figure compares the significant differences between the Pro group and the NPs group). (C, D) Fluorescence microscopy images of Calcein-AM/PI-stained live/dead cells following treatment with propofol and Bai-Fe(III) ICP@Pro NCPs for 4 and 12 h are presented. (E, F) Cell viability of NCM 460 cells after 4 and 12 h of exposure to propofol and Bai-Fe(III) ICP@Pro NCPs is also shown. Statistical significance is indicated as ****P < 0.0001, ***P < 0.001, **P < 0.01, and *P < 0.05.

anesthetic depth, enabling prompt detection of complications and ensuring optimal dosing throughout the anesthetic process [37–39]. In this study, both the TI and vital signs of mice were measured to assess the safety and anesthetic performance of Bai-Fe(III) ICP@Pro NCPs.

3.6.1. *TI*

TI defined as the ratio of the median LD_{50} to the median ED_{50} (TI = LD_{50}/ED_{50}), is a key parameter reflecting a drug's safety margin [40–42], with higher values indicating greater safety due to a wider separation between effective and toxic doses. To evaluate TI, male C57 BL/6 mice (12–16 g) were administered varying concentrations of free propofol or Bai-Fe(III) ICP@Pro NCPs (propofol:baicalin mass ratio = 6:1) via tail vein injection, and the righting reflex and time to death were recorded to determine ED_{50} and LD_{50} using the Bliss method. As shown in Table 1, Bai-Fe(III) ICP@Pro NCPs exhibited a slightly lower ED_{50} than free propofol, indicating

Table 1 – Summary of TI and related parameters.

Groups	ED_{50} (mg/kg)	95% CI (mg/kg)	LD_{50} (mg/kg)	95% CI (mg/kg)	TI
Propofol	10.0	9.2-10.9	42.3	40.0-44.7	4.23
Pro@Fe(III)-Bai ICPs	8.3	7.5-9.1	58.4	56.3-60.6	7.036
Pro@Fe(III)-Bai ICPs+US	4.3	3.8-4.9	36.0	33.8-38.3	8.372

comparable anesthetic potency, while the LD_{50} increased significantly from 42.3 mg/kg (free propofol) to 58.4 mg/kg, demonstrating reduced systemic toxicity. Consequently, the TI increased by 1.66-fold, reflecting the improved safety of the nanocomposite formulation. Notably, the Bai-Fe(III) ICP@Pro NCPs + US group displayed an even lower ED_{50}, approximately half that of free propofol, while achieving a TI of 8.372, substantially higher than both free propofol (TI = 4.23) and Bai-Fe(III) ICP@Pro NCPs alone (TI = 7.036). These results confirm that combining nanocomposites with US-mediated BBB opening not only enhances anesthetic efficacy but also significantly expands the safety margin. Overall, the strategy of using Bai-Fe(III) ICP@Pro NCPs with FUS-MBs enables efficient, low-dose delivery of anesthetics to the brain while simultaneously incorporating neuroprotective agents to mitigate toxicity, providing a synergistic therapeutic effect with promising potential for both experimental and clinical anesthetic applications.

3.6.2. *Physiological indicators*

Monitoring physiological parameters during anesthesia is essential for ensuring patient safety, minimizing risks, and improving surgical outcomes, particularly in high-risk individuals. In this study, the safety and anesthetic performance of different formulations were evaluated in C57BL/6 mice by measuring anesthesia duration, heart rate and blood pressure.

Anesthesia duration was defined as the maintenance phase, representing the interval between the loss and return of the righting reflex following anesthetic administration. Clinically, the goal is to prolong anesthesia duration while minimizing drug dosage. Mice were intravenously injected via the tail vein with 1.5 × ED_{50} (15 mg/kg) of free propofol, Bai-Fe(III) ICP@Pro NCPs, or Bai-Fe(III) ICP@Pro NCPs combined with US. As shown in Fig. 6A, the average anesthesia duration in the free propofol group was 35 ± 3 s. Treatment with Bai-Fe(III) ICP@Pro NCPs significantly extended this duration, and co-administration with US further increased the average anesthesia time to 68 ± 10 s, nearly double that of the free propofol group and over 1.5-fold longer than the nanocomposite-only group. These results highlight the role of US in enhancing BBB permeability and facilitating efficient anesthetic delivery.

Heart Rate Monitoring: Heart rate was continuously monitored post-administration, with measurements starting immediately after injection, followed by a 5 s interval between each measurement. Each data point represents the mean of five animals. As shown in Fig. 6B, control mice exhibited a stable heart rate of approximately 400 beats per minute (bpm), whereas the free propofol group showed wider fluctuations and reduced stability. The Bai-Fe(III) ICP@Pro NCPs group maintained a more consistent heart rate, averaging ~380 bpm, while the Bai-Fe(III) ICP@Pro NCPs + US group exhibited values around 385 bpm, falling between the control and free propofol groups. Notably, the heart rate in the US-treated group returned to baseline more rapidly, indicating enhanced cardiovascular stability and improved autonomic regulation.

Systolic and diastolic blood pressures were measured to evaluate hemodynamic effects. Baseline values in normal mice were approximately 105 mmHg (systolic) and 73 mmHg (diastolic), as shown in Fig. 6C and 6D Administration of free propofol caused greater fluctuations and deviations from baseline, whereas the Bai-Fe(III) ICP@Pro NCPs and Bai-Fe(III) ICP@Pro NCPs + US groups exhibited smoother pressure profiles and more rapid return to physiological norms. As summarized in Table 2, the mean deviation in systolic pressure decreased from 9.44 mmHg (propofol) to 4.64 mmHg (NCPs) and 4.4 mmHg (NCPs + US), while the average diastolic pressure deviation was reduced from 6.16 mmHg to 3.6 mmHg and 2.32 mmHg, respectively. These findings indicate that both nanocomposite treatments enhanced hemodynamic stability, with the US-assisted group providing the most consistent and reliable performance.

Collectively, these results demonstrate that the Bai-Fe(III) ICP@Pro NCPs + US formulation not only significantly prolongs anesthesia duration but also minimizes cardiovascular disturbances. Notably, these benefits were achieved at a lower ED_{50} of propofol (6.45 mg/kg), indicating reduced systemic toxicity and an enhanced therapeutic profile. This strategy provides a safer and more efficient anesthetic platform, with promising potential to improve outcomes in both routine and high-risk surgical settings.

3.7. *Neurotoxicity of propofol during development in vivo*

To evaluate the developmental neurotoxicity of propofol, histopathological analyses of the hippocampal CA1 and CA3 regions were performed using H&E and Nissl staining, allowing visualization of neuronal morphology and assessment of neurodegeneration. As shown in Fig. 7A, H&E staining revealed extensive neuronal loss and architectural disorganization in mice exposed to free propofol for two consecutive days (6 h per day), with neurons in the CA1 and CA3 regions sparsely distributed, irregularly arranged, and exhibiting substantial tissue disruption. In contrast, mice treated with Pro@Fe(III)-Bai ICPs or Pro@Fe(III)-Bai ICPs + US displayed largely preserved hippocampal architecture, with no significant reduction in neuronal density. Although a mild increase in intercellular spacing was observed, overall cellular organization remained intact. Quantitative neuronal injury

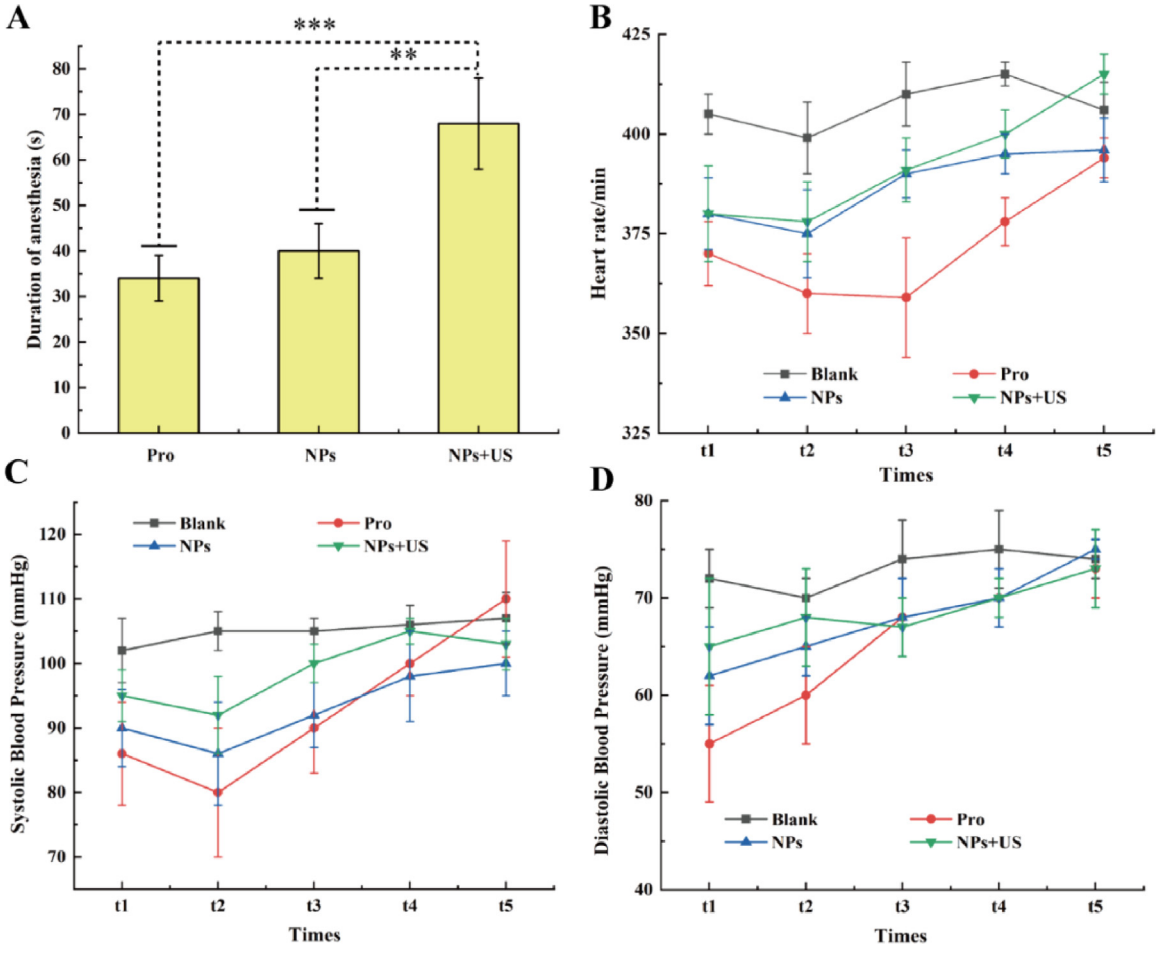


Fig. 6 – Monitoring of different physiological parameters in mice following various treatments. (A) Anesthesia duration in mice after different treatments ($n = 5$). (B) Heart rate and mean differences in mice across treatment groups ($n = 5$). (C, D) Diastolic and systolic blood pressures of mice following different treatments ($n = 5$). Statistical significance is indicated as ***$P < 0.001$ and **$P < 0.01$).

Table 2 – Summary of mean difference in heart rate and blood pressure in each group.

Physiological indicators	Blank	Propofol	Bai-Fe(III) ICP@Pro NCPs	Bai-Fe(III) ICP@Pro NCPs+US
Heart rate	4.4	11.4	7.76	11.76
Systolic pressure	1.2	9.44	4.64	4.4
Diastolic pressure	1.6	6.16	3.6	2.32

scoring (Fig. 7B and 7C) corroborated these observations, showing that damage scores in the free propofol group were over fivefold higher than those in the Pro@Fe(III)-Bai ICPs and Pro@Fe(III)-Bai ICPs + US groups across both hippocampal subregions. While the propofol group exhibited significantly elevated damage compared with controls [39], there was no statistically significant difference between the nanocomposite and nanocomposite + US groups, indicating that the neuroprotective effect of baicalin within the ICP nanocomposite system is preserved regardless of US exposure.

Nissl staining (Fig. 7D) further confirmed these observations. In the free propofol group, neuronal degeneration was pronounced, with a marked reduction in Nissl bodies and decreased neuronal density in both CA1 and CA3 regions. In contrast, mice treated with Bai-Fe(III) ICP@Pro NCPs or Bai-Fe(III) ICP@Pro NCPs + US maintained relatively intact Nissl body structures, indicating preserved neuronal function and morphology. Quantitative analysis (Fig. 7E and 7F) showed that Nissl body counts in the free propofol group were approximately half of those in the control group, whereas the two nanocomposite-treated groups exhibited counts around 87% of the control, with no significant difference between them, and significantly higher than the free propofol group. Collectively, the H&E and Nissl staining results demonstrate that repeated

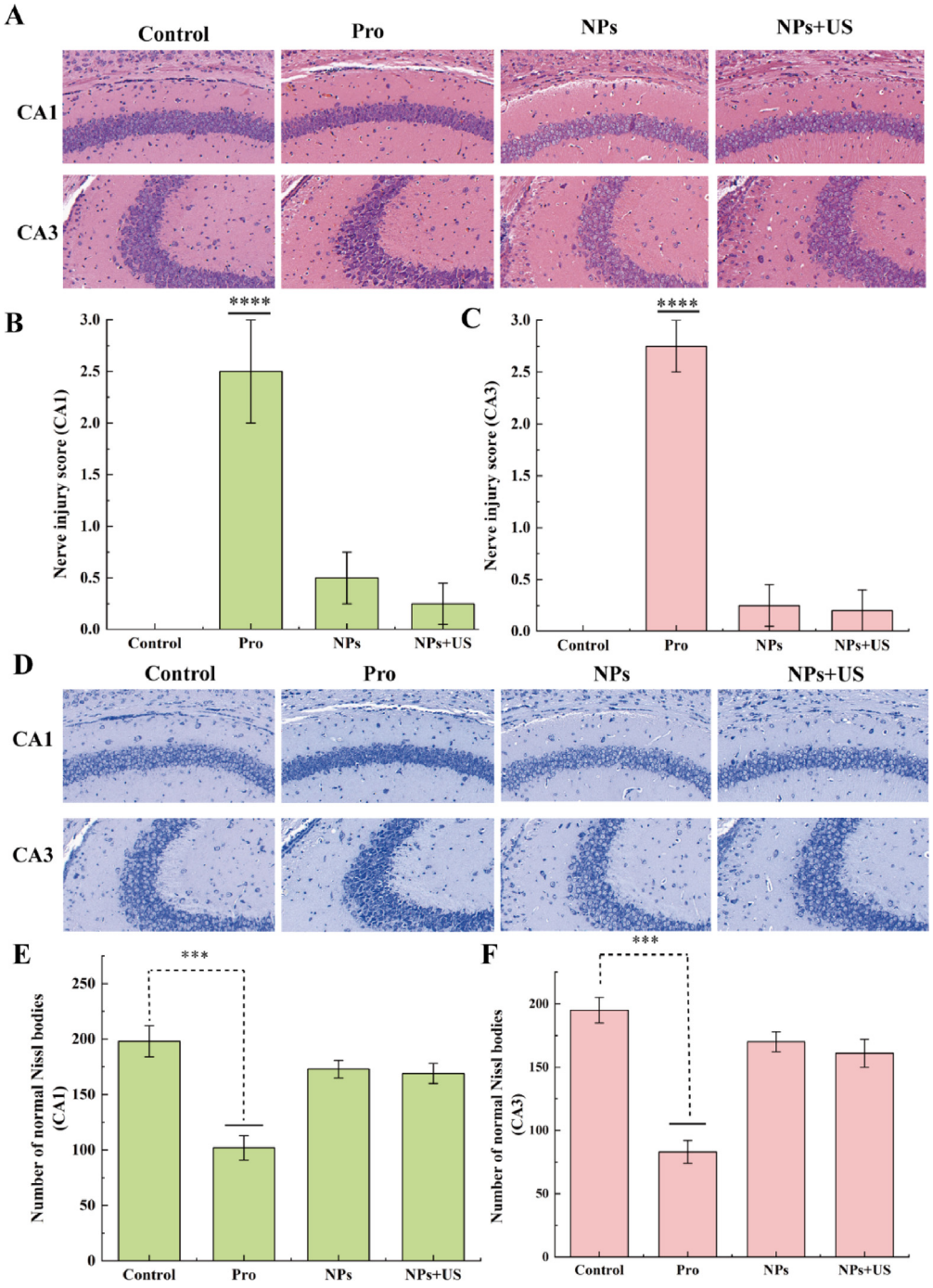


Fig. 7 – H&E and Nissl staining of hippocampal CA1 and CA3 regions in young mice following treatment with different drug formulations. (A) H&E staining of CA1 and CA3 regions. (B) Quantification of neuronal injury scores in the CA1 region. (C) Quantification of neuronal injury scores in the CA3 region (The score ranges from 0 to 5, and the consistency of the reviewers is over 90%). (D) Nissl staining of CA1 and CA3 regions. (E) Number of Nissl bodies in the CA1 region. (F) Number of Nissl bodies in the CA3 region. Statistical significance is indicated as ****$P < 0.0001$ and ***$P < 0.001$.

exposure to free propofol during early development induces substantial hippocampal neurodegeneration, particularly in the CA1 and CA3 regions, which are critical for learning and memory. Encapsulation of propofol within Bai-Fe(III) ICP nanocomposites markedly mitigates these neurotoxic effects, highlighting the therapeutic potential of this nanoplatform in reducing anesthesia-induced developmental neurotoxicity.

3.8. *Behavioral assessment of neurocognitive function*

To evaluate the impact of anesthetic nanocomposites on neurocognitive development, behavioral tests, including the OFT, novel object recognition, and Y-maze, were conducted in young mice [43,44] to assess locomotor activity, exploratory behavior, and cognitive performance following treatment.

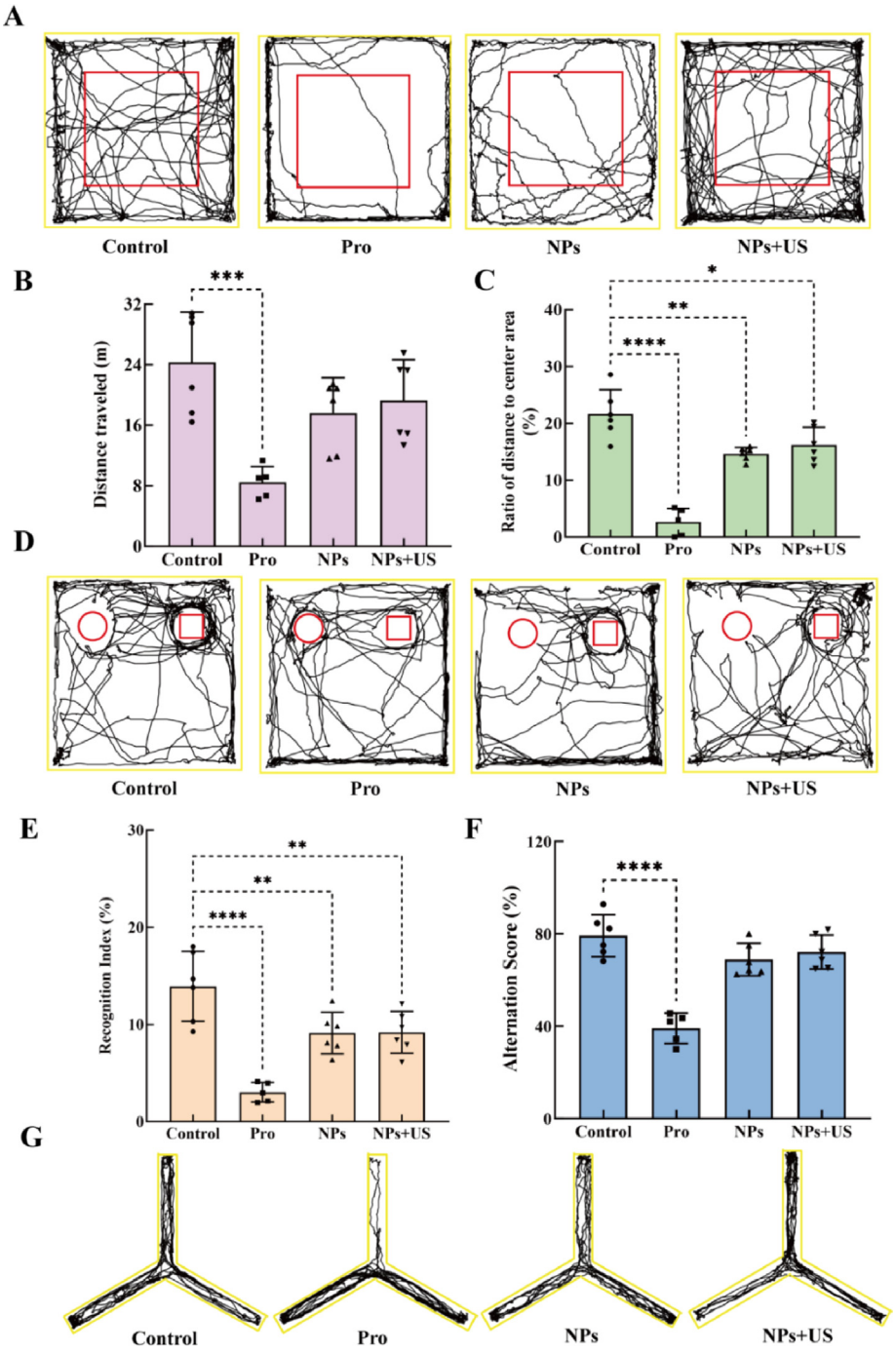


Fig. 8 – Effect of different drug treatments on cognitive function in young mice. (A) Trajectory map of the OFT. (B) Total distance traveled in the OFT. (C) Proportion of distance traveled within the central area during the OFT. (D) Trajectory map for the NORT. (E) Proportion of time spent investigating novel objects in the recognition test. (F) Percentage of spontaneous alternations in the Y-maze test. (G) Trajectory map in the Y-maze test. Data are presented as mean ± SD ($n = 6$), with statistical significance indicated as ****$P < 0.0001$, ***$P < 0.001$, **$P < 0.01$, and *$P < 0.05$.

In the OFT, total distance traveled served as an indicator of general locomotor function and depression-like behavior, while movement within the central grid reflected anxiety-related responses and exploratory curiosity [44,45]. As shown in Fig. 8A, mice treated with free propofol (Pro) exhibited markedly reduced overall locomotion, with both total distance and central zone movement significantly lower than those of the control group. Quantitatively, the control group traveled an average of 24 ± 3.6 m in 5 min, whereas the free propofol group covered only 8 m, approximately one-third of control activity (Fig. 8B). In contrast, mice treated with Bai-Fe(III) ICP@Pro NCPs or Bai-Fe(III) ICP@Pro NCPs + US maintained higher activity

levels, traveling over 16 m, indicating substantial preservation of motor function.

Exploration within the central zone further highlighted behavioral differences among the groups. Mice exposed to free propofol exhibited minimal central area activity, covering only 2.5% of their total distance in this zone. In contrast, the Bai-Fe(III) ICP@Pro NCPs and Bai-Fe(III) ICP@Pro NCPs + US groups displayed central zone activity of 14% and 16%, respectively, approaching that of the control group (21%) (Fig. 8C). These results indicate that free propofol induced anxiety-like and depressive behaviors along with impaired motor activity in developing mice. Conversely, treatment with the nanocomposite formulation-with or without ultrasound-significantly alleviated these behavioral deficits, with the ultrasound-enhanced group demonstrating the most pronounced improvement, including a reduction in anxiety-related behaviors. Collectively, these findings demonstrate that encapsulation of propofol within Bai-Fe(III) ICP nanocomposites substantially mitigates behavioral impairments associated with developmental exposure to free propofol, and that US further enhances this protective effect, likely through improved drug delivery and reduced systemic toxicity. Cognitive performance was further evaluated using the novel object recognition and Y-maze tests, which assess recognition memory and spatial working memory, respectively [43,45].

In the NORT, the RI quantified the animals' ability to distinguish between familiar and novel objects, with higher RI values reflecting enhanced memory and exploratory behavior [46]. As shown in Fig. 8D, mice treated with free propofol spent markedly less time exploring novel objects compared to controls, indicating impaired recognition memory. Quantitative analysis (Fig. 8E) revealed an RI of only 2.9% in the propofol group, significantly lower than the 13.5% observed in the control group. In contrast, mice treated with Bai-Fe(III) ICP@Pro NCPs and Bai-Fe(III) ICP@Pro NCPs + US achieved RI values reaching approximately 65.0% ± 6.5% of the control group, demonstrating significant recovery of recognition memory. The Y-maze test was used to evaluate spatial memory and decision-making, with the percentage of spontaneous alternations serving as the primary indicator [47]. This score was less than half that of the control group, which exhibited an average alternation rate of 80.0% ± 8.3% (Fig. 8G), indicating that spatial memory was impaired. However, the Bai-Fe(III) ICP@Pro NCPs and Bai-Fe(III) ICP@Pro NCPs + US groups achieved alternation scores around 69.8% ± 5.3%, not significantly different from controls, suggesting substantial preservation of cognitive ability. Collectively, these behavioral analyses demonstrate that prolonged developmental exposure to free propofol causes marked impairments in recognition and spatial working memory. Encapsulation of propofol within Bai-Fe(III) ICP nanocomposites significantly mitigates these neurotoxic effects, and US-enhanced delivery further improves outcomes, likely via facilitated BBB penetration and more effective CNS drug distribution. These findings hold important implications for future clinical applications of nanocomposites, offering a promising strategy to reduce long-term neurodevelopmental risks associated with continuous propofol infusion in anesthesia

4. Conclusion

In this study, we developed a strategy by combining neuroprotective of baicalin with propofol anesthesia, utilizing high propofol-loaded porous Baicalin-Fe(III) infinite coordination polymer nanocomposites (Bai-Fe(III) ICP@Pro NCPs), with a propofol loading capacity of 62.8%. When integrated with US-mediated microbubble cavitation, this approach significantly enhanced BBB permeability and propofol delivery, resulting in a twofold increase in the TI and a substantially widened safety margin compared with free propofol. Notably, anesthesia duration was nearly doubled, indicating that equivalent anesthetic efficacy could be achieved at significantly reduced doses. Physiological monitoring demonstrated improved cardiovascular stability, with heart rate and blood pressure closer to control levels in mice treated with Bai-Fe(III) ICP@Pro NCPs + US. Histological evaluations revealed that free propofol induced marked neurotoxicity in developing mice, characterized by neuronal loss, disrupted hippocampal architecture, and diminished Nissl body density, whereas Bai-Fe(III) ICP@Pro NCPs effectively mitigated these effects. Behavioral analyses further supported these findings, showing significant improvements in motor activity, spatial memory, and cognitive function in the nanocomposite-treated groups. The alternation scores were around 69.8% ± 5.3%, and the RI value reached approximately 65.0% ± 6.5% of the control group, with motor activity almost fully restored, underscoring baicalin's neuroprotective synergy in recovering propofol-induced irreversible developmental neurotoxicity. Collectively, these results underscore the potent neuroprotective efficacy of baicalin and the synergistic benefits of US-enhanced propofol brain delivery. The proposed Bai-Fe(III) ICP@Pro NCPs-based strategy holds substantial promise for safer, long-term propofol anesthesia, particularly in vulnerable populations such as developing individuals. Future clinical trials to assess human efficacy will be essential to validate these findings and offer a valuable direction for clinical translation.

Conflicts of interest

The authors declare that there is no conflicts of interest. The authors alone are responsible for the content and writing of this article.

CRediT authorship contribution statement

Shuo Zhang: Writing – original draft, Methodology, Formal analysis, Conceptualization. **Lei Shi:** Investigation, Data curation. **Jiansheng He:** Resources, Formal analysis. **Ji Xia:** Validation, Methodology. **Shunlian Li:** Resources, Data curation. **Rong Wang:** Methodology, Formal analysis. **Qingyan Ma:** Resources, Data curation. **Mingting Zhu:** Resources, Investigation. **Peng Tang:** Methodology, Investigation. **Hao Tian:** Validation, Data curation. **Feiqian Wang:** Methodology, Conceptualization. **Mingxi Wan:** Supervision, Formal analysis. **Daocheng Wu:** Writing – review & editing, Methodology, Conceptualization. **Wei Gao:** Investigation, Conceptualization.

Xiancang Ma: Supervision, Methodology, Funding acquisition. **Feng Zhu:** Resources, Funding acquisition.

Acknowledgments

This work was funded by the National Natural Science Foundation of China (No. 82271572), The Clinical Research Award of the First Affiliated Hospital of Xi'an Jiaotong University (No. XJTU1AF2021CRF-008) and (No. XTJU1AF-CRF-2023-025). The authors thank Huimin Tong and Ying Hao and acknowledge the support from the core facilities and experiment center of Xi'an Jiaotong University.

Supplementary materials

Supplementary material associated with this article can be found, in the online version, at doi:10.1016/j.ajps.2026.101117. The figures and tables with "S" before the serial number are included in the Supplementary data.

References

[1] Walsh CT. Propofol: milk of amnesia. Cell 2022;185(25):4861.
[2] Han RH, Huang HM, Han H, Chen H, Zeng F, Xie X, et al. Propofol postconditioning ameliorates hypoxia/reoxygenation induced H9c2 cell apoptosis and autophagy via upregulating forkhead transcription factors under hyperglycemia. Mil Med Res 2021;8(1):58.
[3] Kotani Y, Pruna A, Turi S, Borghi G, Lee TC, Zangrillo A, et al. Propofol and survival: an updated meta-analysis of randomized clinical trials. Crit Care 2023;27(1):139.
[4] Olutoye OA, Baker BW, Belfort MA, Olutoye OO. Food and Drug Administration warning on anesthesia and brain development: implications for obstetric and fetal surgery. Am J Obstet Gynecol 2018;218(1):98–102.
[5] Zhang TY, Ji DF, Sun JY, Song JL, Nie LM, Sun N. NPAS4 suppresses propofol-induced neurotoxicity by inhibiting autophagy in hippocampal neuronal cells. Arch Biochem Biophys 2021;711:109018.
[6] Tang F, Zhao LL, Yu Q, Liu TY, Gong HY, Liu ZY, et al. Upregulation of miR-215 attenuates propofol-induced apoptosis and oxidative stress in developing neurons by targeting LATS2. Mol Med 2020;26(1):38.
[7] Li WW, Cheng LZ, Zou Z, Tian ML, Zhang H, Raya AD, et al. (R)-alpha-methylhistamine suppresses inhibitory neurotransmission in hippocampal CA1 pyramidal neurons counteracting propofol-induced amnesia in rats. CNS Neurosci Ther 2014;20(9):851–9.
[8] Xing N, Xing F, Li YN, Li PL, Zhang JW, Wang DM, et al. Dexmedetomidine improves propofol-induced neuronal injury in rat hippocampus with the involvement of miR-34a and the PI3K/Akt signaling pathway. Life Sci 2020;247:117359.
[9] Udrea AM, Gradisteanu Pircalabioru G, Boboc AA, Mares C, Dinache A, Mernea M, et al. Advanced bioinformatics tools in the pharmacokinetic profiles of natural and synthetic compounds with anti-diabetic activity. Biomolecules 2021;11(11):1692.
[10] Ding XW, Sun X, Shen XF, Lu Y, Wang JQ, Sun ZR, et al. Propofol attenuates TNF-α-induced MMP-9 expression in human cerebral microvascular endothelial cells by inhibiting Ca^{2+}/CAMK II/ERK/NF-κb signaling pathway. Acta Pharmacol Sin 2019;40(10):1303–13.
[11] Chen W, Ju XZ, Lu Y, Ding XW, Miao CH, Chen JW. Propofol improved hypoxia-impaired integrity of blood-brain barrier via modulating the expression and phosphorylation of zonula occludens-1. CNS Neurosci Ther 2019;25(6):704–13.
[12] Wang C, Wang S, Wu C, Lei L, Wang DX, Zhang Q. Physical and chemical compatibility of etomidate and propofol injectable emulsions. Pharmacology 2021;106(11–12):644–57.
[13] Nilsson N, Nezvalova-Henriksen K, Tho I. Emulsion stability of different intravenous propofol formulations in simulated co-administration with remifentanil hydrochloride. Pharm Technol Hosp Pharm 2019;4(2):77–87.
[14] Visvabharathy L, Xayarath B, Weinberg G, Shilling RA, Freitag NE. Propofol increases host susceptibility to microbial infection by reducing subpopulations of mature immune effector cells at sites of infection. PLoS One 2015;10(9):e0138043.
[15] Chaki T, Hirata N, Yoshikawa Y, Tachibana S, Tokinaga Y, Yamakage M. Lipid emulsion, but not propofol, induces skeletal muscle damage and lipid peroxidation. J Anesth 2019;33(6):628–35.
[16] Li Y, Wang B, Zhang LL, He SF, Hu XW, Wong GTC, et al. Dexmedetomidine combined with general anesthesia provides similar intraoperative stress response reduction when compared with a combined general and epidural anesthetic technique. Anesth Analg 2016;122(4):1202–10.
[17] Du YT, Li YW, Zhao BJ, Guo XY, Feng Y, Zuo MZ, et al. Long-term survival after combined epidural-general anesthesia or general anesthesia alone: follow-up of a randomized trial. Anesthesiology 2021;135(2):233–45.
[18] Li YW, Li HJ, Li HJ, Zhao BJ, Guo XY, Feng Y, et al. Delirium in older patients after combined epidural-general anesthesia or general anesthesia for major surgery: a randomized trial. Anesthesiology 2021;135(2):218–32.
[19] Sridharan K, Sivaramakrishnan G. Comparison of fentanyl, remifentanil, sufentanil and alfentanil in combination with propofol for general anesthesia: a systematic review and meta-analysis of randomized controlled trials. Curr Clin Pharmacol 2019;14(2):116–24.
[20] Hassani Najafabadi A, Azodi-Deilami S, Abdouss M, Payravand H, Farzaneh S. Synthesis and evaluation of hydroponically alginate nanoparticles as novel carrier for intravenous delivery of propofol. J Mater Sci Mater Med 2015;26(3):145.
[21] Zhang S, Wang YS, Zhu MT, Liu BY, Zhao WP, Zhang S, et al. Ultrasound combined blood-brain barrier targeting brain delivery of four-in-one molecular aggregates for the enhancement of anesthetic efficacy and toxicity reduction via propofol-etomidate synergistically inhibition GABA receptor. Aggregate 2024;5(5):e573.
[22] McMahon D, O'Reilly MA, Hynynen K. Therapeutic agent delivery across the blood-brain barrier using focused ultrasound. Annu Rev Biomed Eng 2021;23(1):89–113.
[23] Zhao PX, Wu TT, Tian Y, You J, Cui XW. Recent advances of focused ultrasound induced blood-brain barrier opening for clinical applications of neurodegenerative diseases. Adv Drug Deliv Rev 2024;209:115323.
[24] Curley CT, Stevens AD, Mathew AS, Stasiak K, Garrison WJ, Miller GW, et al. Immunomodulation of intracranial melanoma in response to blood-tumor barrier opening with focused ultrasound. Theranostics 2020;10(19):8821–33.
[25] Shen YY, Hu MN, Li W, Chen YL, Xu YL, Sun LT, et al. Delivery of DNA octahedra enhanced by focused ultrasound with microbubbles for glioma therapy. J Control Rel 2022;350:158–74.
[26] Moore-Palhares D, Dasgupta A, Saifuddin M, Anzola Pena ML, Prasla S, Ho L, et al. Radiation enhancement using focussed ultrasound-stimulated microbubbles for breast cancer: a phase 1 clinical trial. PLoS Med 2024;21(5):e1004408.

[27] Li YF, Zhang YF, Huang C, Jiang JM. Baicalin improves neurological outcomes in mice with ischemic stroke by inhibiting astrocyte activation and neuroinflammation. Int Immunopharmacol 2025;149:114186.
[28] Yang JL, Jia ZX, Xiao ZG, Zhao J, Lu Y, Chu L, et al. Baicalin rescues cognitive dysfunction, mitigates neurodegeneration, and exerts anti-epileptic effects through activating TLR4/MYD88/Caspase-3 pathway in rats. Drug Des Devel Ther 2021;20(15):3163–80.
[29] Liu ZSJ, Truong TTT, Bortolasci CC, Spolding B, Panizzutti B, Swinton C, et al. The potential of baicalin to enhance neuroprotection and mitochondrial function in a human neuronal cell model. Mol Psychiatry 2024;29(8):2487–95.
[30] Zheng WX, He WQ, Zhang QR, Jia JX, Zhao S, Wu FJ, et al. Baicalin inhibits NLRP3 inflammasome activity via the AMPK signaling pathway to alleviate cerebral ischemia-reperfusion injury. Inflammation 2021;44(5):2091–105.
[31] Zhang L, Miao CY, Wang ZX, Guan XL, Ma YC, Song JY, et al. Preparation and characterisation of baicalin magnesium and its protective effect in ulcerative colitis via gut microbiota-bile acid axis modulation. Phytomedicine 2024;126: 155416.
[32] Alnasraui AHF, Joe IH, Al-Musawi S. Design and synthesize of folate decorated Fe_3O_4@Au-DEX-CP nano formulation for targeted drug delivery in colorectal cancer therapy: *in vitro* and *in vivo* studies. J Drug Deliv Sci Technol 2023;87:104798.
[33] Abdulwahid FS, Haider AJ, Al-Musawi S. Effect of laser parameter on Fe_3O_4 NPs formation by pulsed laser ablation in liquid. AIP Conf Proc 2023;2769:020039.
[34] Haider AJ, Al-Kinani MA, Al-Musawi S. Preparation and characterization of gold coated super paramagnetic iron nanoparticle using pulsed laser ablation in liquid method. Key Eng Mater 2021;886:77–85.
[35] Chen J, Escoffre JM, Romito O, Iazourene T, Presset A, Roy M, et al. Enhanced macromolecular substance extravasation through the blood-brain barrier via acoustic bubble-cell interactions. Ultrason Sonochem 2024;103:106768.
[36] Zhu MT, Wu PY, Li Y, Zhang L, Zong YJ, Wan MX. Synergistic therapy for orthotopic gliomas via biomimetic nanosonosensitizer-mediated sonodynamic therapy and ferroptosis. Biomater Sci 2022;10(14):3911–23.
[37] Laferrière-Langlois P, Morisson L, Jeffries S, Duclos C, Espitalier F, Richebé P. Depth of anesthesia and nociception monitoring: current state and vision for 2050. Anesth Analg 2024;138(2):295–307.
[38] Roche D, Mahon P. Depth of anesthesia monitoring. Anesthesiol Clin 2021;39(3):477–92.
[39] Brook K, Agarwala AV, Li F, Purdon PL. Depth of anesthesia monitoring: an argument for its use for patient safety. Curr Opin Anaesthesiol 2024;37(6):689–96.
[40] Filimonova M, Saburova A, Shevchenko L, Makarchuk V, Shitova A, Soldatova O, et al. 1-isobutanoil-2-isopropylisothiourea phosphate, T1082: a safe and effective prevention of radiotherapy complications in oncology. Int J Mol Sci 2022;23(5):2697.
[41] Li ZY, Xiao XY, Xue YL, Zhou HL, Huang CN, Zhu M, et al. Discovery of a novel class of benzoxazole derivatives as histamine H3 receptor ligands for the treatment of neuropathic pain. Bioorg Chem 2022;127:106039.
[42] Mehta M, Allen-Gipson D, Mohapatra S, Kindy M, Limayem A. Study on the therapeutic index and synergistic effect of Chitosan-zinc oxide nanomicellar composites for drug-resistant bacterial biofilm inhibition. Int J Pharm 2019;565:472–80.
[43] Xiong S, Li ZJ, Liu Y, Wang Q, Luo JS, Chen XJ, et al. Brain-targeted delivery shuttled by black phosphorus nanostructure to treat Parkinson's disease. Biomaterials 2020;260:120339.
[44] Li LJ, Sun XY, Huang YR, Lu S, Xu YM, Yang J, et al. Neuronal double-stranded DNA accumulation induced by DNase II deficiency drives tau phosphorylation and neurodegeneration. Transl Neurodegener 2024;13(1):1–17.
[45] Liu XY, Zhao YC, Dou JB, Hou QH, Cheng JX, Jiang XY. Bioeffects of inhaled nanoplastics on neurons and alteration of animal behaviors through deposition in the brain. Nano Lett 2022;22(3):1091–9.
[46] Sadegzadeh F, Sakhaie N, Dehghany R, Adak O, Saadati H. Effects of adolescent administration of fluoxetine on novel object recognition memory, anxiety-like behaviors, and hippocampal brain-derived neurotrophic factor level. Life Sci 2020;260:118338.
[47] Farokhcheh M, Hejazian L, Akbarnejad Z, Pourabdolhossein F, Hosseini SM, Mehraei TM, et al. Geraniol improved memory impairment and neurotoxicity induced by zinc oxide nanoparticles in male Wistar rats through its antioxidant effect. Life Sci 2021;282:119823.